Microstructures

Review

Phase-dependent materials design and characteristic properties of two-dimensional (2D) halide perovskite single crystals for optoelectronic applications

Su-Min Lee[1] iD**, Mang Muan Lian[1]** iD**, Su-Ho Ahn[1], Dong-Jun Yeon[1], Younghee Jang[1], EQ Han[2], Yurou Zhang[2,3], Jung-Hoon Sul[4], Jung-Ho Yun[1]** iD

[1]Air & Environment Energy Nexus (A2EN) Lab, Department of Environmental Science and Engineering, College of Engineering, Kyung Hee University, Gyeonggi-do 17104, Republic of Korea.
[2]Nanomaterials Centre, Australian Institute for Bioengineering and Nanotechnology (AIBN), School of Chemical Engineering, The University of Queensland, Queensland 4027, Australia.
[3]Zhejiang Baima Lake Laboratory Co., Ltd, Hangzhou 310000, Zhejiang, China.
[4]School of Engineering and Technology, Central Queensland University, Queensland 4740, Australia.

Correspondence to: Prof. Jung-Ho Yun, Air & Environment Energy Nexus (A2EN) Lab, Department of Environmental Science and Engineering, College of Engineering, Kyung Hee University, 1732, Deogyeong-daero, Giheung-gu, Yongin-si, Gyeonggi-do 17104, Republic of Korea. E-mail: jungho.yun@khu.ac.kr

Abstract

Two-dimensional organic-inorganic hybrid halide perovskites have garnered much attention owing to their outstanding stability alongside unique quantum-well structures and anisotropic properties, leading to improved charge dynamics. Two-dimensional perovskites can be divided into three phases including Ruddlesden-Popper, Dion-Jacobson, and Alternating cations in the interlayer space phase. Each phase of these perovskites shows distinguished phase-dependent structural and optoelectrical properties. Tuning their properties by designing the materials can be a key strategy to enhance the device performance in optoelectrical applications. Configuration of spacer cations and the control of octahedral layer numbers (*n*) can be important parameters in material design, enabling the tuning of dielectric properties, exciton binding energy, and bandgaps, as well as materials structures, thereby influencing stability and charge transport behaviors. In this point, two-dimensional perovskite single crystals can play essential roles in not only understanding phase-dependent intrinsic natures but also enhancing

performance of optoelectronic applications, specifically owing to their long carrier diffusion length and enhanced stability with little grain boundaries and low trap density. This review will deliver the strategy of phase-dependent materials design with an understanding of their anisotropic properties and charge dynamics for optoelectronic applications, including photodetectors and X-ray detectors.

Keywords: Two-dimensional organic-inorganic hybrid halide perovskites (2D OIHPs), perovskite single crystals, anisotropic properties, RP phase, DJ phase, ACI phase

INTRODUCTION

Organic-inorganic hybrid halide perovskites (OIHPs) with the 3D ABX_3 structure [A: CH_3NH_3, $HC(NH_2)_2$, Cs; B: Pb, Sn; X: I, Br, Cl] have been attracting great attention due to the outstanding materials properties with the high-performance demonstration of 26.7% in solar cell applications where one of critical points in determining the performance of the high-efficiency perovskite solar cells is the passivation strategy to suppress ion migration and facilitate the charge dynamics[1]. Representatively, the *in-situ* employment of long-chained cation-based two-dimensional (2D) perovskite layers to the solar cell fabrication demonstrated the effective passivation strategy to significantly minimize the ion migration of halide ions within perovskite active layers, resulting in the low performance and poor stability[2]. It is clearly shown that the 2D perovskites play a key role as excellent passivation additives in perovskite solar cell development. Additionally, interest in unique materials properties of these perovskites is growing with the promise of their potential expanded to diverse optoelectronic applications, beyond the passivation layer role limited to perovskite solar cells. Recently, 2D perovskites have been reported with diverse optoelectronic applications such as photodetectors[3], X-ray detectors[4], light emitting diodes[5] and photovoltaics[6,7], owing to more enhanced stability, ion migration suppression, and charge dynamics, compared with 3D perovskites[7,8]. These excellent material features of 2D perovskites originate from the unique sequential configuration of organic and inorganic layers in the stacked 2D perovskite structures with high tuneability of cations. The organic parts in 2D perovskites mainly contribute to improving the stability with humidity and oxygen tolerant properties by preventing moisture penetration and ion migration[9]. In addition, different dielectric levels between these organic insulating layers and inorganic layers can create quantum-well structures. These layered structures exhibit strong anisotropic properties in charge behaviors where the controlled quantum-well thickness with the number (n) of BX_6 layers can tune bandgap and carrier transport properties. Aside from inorganic layer thickness, diversity of organic cations can also induce diverse structural and material properties including dielectric characteristics and charge transport. Most interestingly, various synthetic methodologies combined with chemical composition engineering allow the phase control of 2D perovskites. This phase modulation enables more specific tuning of their material properties. Most of the studies focus on (100)-oriented phases including Ruddlesden-Popper (RP), Dion-Jacobson (DJ), and Alternating cations in the interlayer space (ACI) phases[10]. Depending on the phases of 2D perovskites, bonding types of organic layers and the resulting quantum-well structures are altered, affecting the physicochemical and optoelectrical properties. Thus, it is important to understand the mechanism of forming and controlling the phases in designing 2D-based high-performing materials and device applications. One of the best ways to understand the phases of 2D perovskites in depth is to study their intrinsic material properties at the level of single crystal forms. Perovskite single crystals have lower defect densities, fewer bulk trap sites, and no grain boundaries, while polycrystalline perovskite films comprise various defect sources that can result in ambiguousness in understanding the correlation between device performance and materials properties. Due to these properties, 2D single crystals can show enhanced chemical stability and optical properties in optoelectronic applications. Therefore, these crystals can be an ideal platform not only to explore the intrinsic materials natures of 2D perovskites but also to fabricate 2D perovskite-based high-performance optoelectronic applications. Low-dimensional OIHP single crystals,

including not only 2D but 1D and 0D, also have remarkable optoelectronic and anisotropic properties. However, 0D and 1D single crystals face difficulties revealing the photoelectrical properties including charge behavior on excited states, and photoluminescence (PL) mechanism of 0D remains widely controversial. Additionally, materials design principles for 0D and 1D perovskites are not well defined, largely owing to the influence of isolated octahedra and clusters[11,12]. The relatively large bandgaps and greater defect densities compared to 2D perovskites further limit their direct use in optoelectronic applications. In this review, we will investigate comprehensive anisotropic properties of 2D OIHPs in the form of single crystals, and identify the unique structures, followed by optoelectrical characteristics of each phase. Phase-dependent materials design strategies will also be suggested with respect to the configuration of organic cations and tuning the inorganic layer thickness (*n*). Additionally, their applications will be reviewed based on the recently published papers for materials design and applications.

INTRINSIC NATURES OF 2D PEROVSKITE SINGLE CRYSTALS

Quantum-well structures of 2D perovskites induce directional dependent properties between the crystallographic planes (in-plane) and cross-plane (out-of-plane). This inherent anisotropy is revealed in directional charge transports and light interaction capabilities. In crystallography, 2D perovskites are oriented from 3D perovskites by slicing down along the planes which are generally <001> planes. As depicted in Figure 1A, by inserting large organic spacers in 3D perovskite structures, the organic spacer can be intolerable to a structure formed by four inorganic octahedrons, so that Goldschmidt tolerance factor (*t*) is out of range of typical 3D perovskites (about 0.8 to 1.1)[13-15]. In a word, 2D perovskites have alternately layered structures which are stacked with organic layers and octahedral layers in the out-of-plane direction. In this layered structure, inorganic potential wells and organic potential barriers build a unique quantum-well structure [Figure 1B]. As a result, 2D perovskite single crystals have distinguished intrinsic properties depending on the direction, in-plane or stacked out-of-plane. These anisotropy properties originating multi-quantum-well structures can be compared to isotropic properties in 3D perovskites, and the character of organic cations also affects them. Since 2D perovskites are not constrained by the tolerance factor (*t*), they are free from space limitations and enable a broad selectivity of spacer cations. The chain length of the spacer cation and the dielectric constant of the organic layer can influence the crystal structural stability, and anisotropic properties including diverse optoelectrical characteristics. In the 2D perovskite system, organic insulating layers have lower permittivity than inorganic layers, and excited charges are confined in the inorganic layers, which can lead to high exciton binding energy of 2D perovskites. Alternating dielectric constants in the quantum well structure affect the electrostatic force of the electron-hole pairs in the excitons. The modulus of this attractive electrostatic force (*F*) depends on the physical distance between the electron and hole (*r*), and the dielectric constant of the lattice (*ε*) along with constant elementary charge (*e*) as given in

$$F = -\frac{1e^2}{4\pi\varepsilon r^2} \tag{1}$$

The low dielectric constants of organic spacers reduce the dielectric shielding effect and enhance the electrostatic force, which can lead to high exciton binding energy. The increase in exciton binding energy resulting from dielectric difference is referred to as dielectric confinement. Although a large exciton binding energy can restrict carrier transport, large organic spacers can prevent internal ion migrations and strengthen the hydrophobicity of the materials. Owing to this dielectric gap between organic and inorganic layers, dielectric confinement and quantum confinement effects should be considered in 2D perovskite systems [Figure 1C]. Rytova and Keldysh explored it theoretically for thin semiconductor films alternately stacked with two layers of different dielectric constants[16-18], and Keldysh's formula for 1 s excitons related to
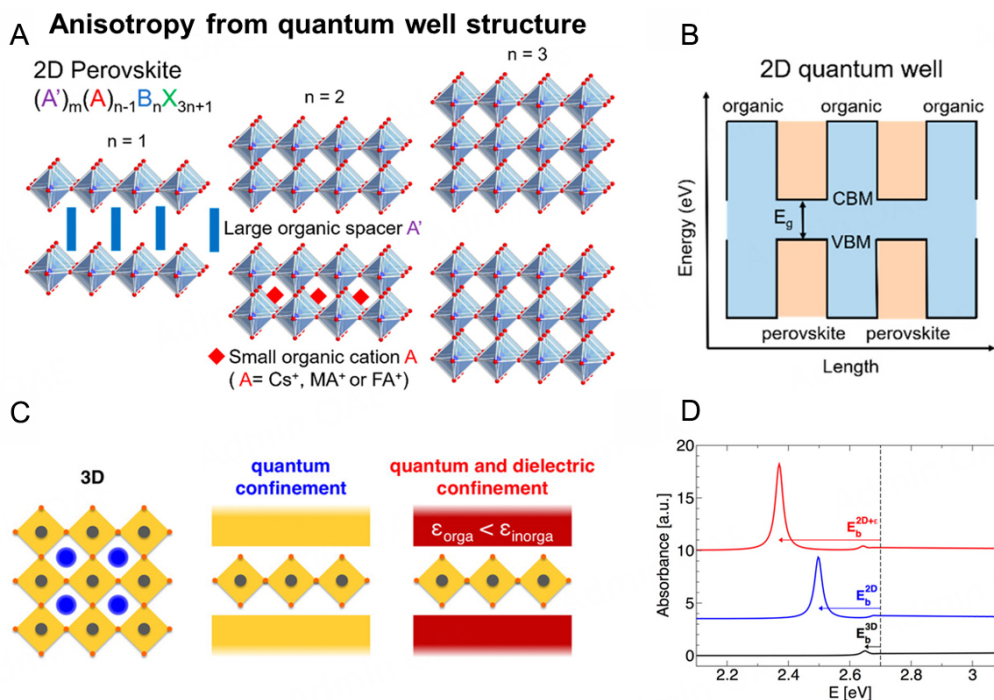
Figure 1. Quantum and dielectric confinement effects of 2D perovskites. (A and B) Schematic illustration of (A) anisotropic properties and (B) 2D quantum well structure of 2D perovskites. Reprinted with permission from ref.[15]: Copyright 2019, American Chemical Society. (C) Schematic illustration of quantum confinement and incorporation of quantum and dielectric confinement. (D) Simulated result of optical absorption from quantum confinement and dielectric confinement due to 1 s excitons. The black line is the optical absorption of the 3D halide perovskite, the blue line is of the 2D with only quantum confinement, and the red line is of the 2D with both quantum and dielectric confinement. Reprinted with permission from ref.[20]: Copyright 2016, American Chemical Society.

the exciton binding energy in a 2D quantum-well structure can be expressed in[19]:

$$E_b^{2D+\varepsilon} = 4(\frac{\varepsilon_w}{\varepsilon_b})^2 E_b^{3D} \qquad (2)$$

The optical absorption was simulated using the $k \cdot p$/BSE approach, so as to clarify the dielectric effects with dimensionality[20]. As shown in Figure 1D, when moving from a 3D to 2D structure, the exciton binding energy rises from 50 to 200 meV and the optical absorption is amplified at the exciton resonance. The blue line shows the particular impact of quantum confinement on the exciton, and the red line represents an estimated huge exciton binding energy with 330 meV, which also includes the dielectric confinement.

The thickness of the inorganic layer (*n*) can also affect those anisotropic properties in quantum well structures. The coupling effect between the electrons and holes lessens as the thickness of the inorganic layer increases, which can lead to increasing exciton transport distance and decreasing exciton density and binding energy. Additionally, the substitution of halide with rising atomic size (Cl < Br < I) can result in a smaller bandgap, which mainly alters valence band energy[21]. Configuration of spacer cations and halide ions with control of the number of octahedral layers can be crucial strategies to enhance charge transport and optoelectrical properties and tune the dielectric properties and bandgaps. Based on these strategies, it is crucial to make proper materials design depending on targeted applications and figure out phase-dependent anisotropic properties for better device performances.

MATERIALS DESIGN METHODS OF 2D PEROVSKITE SINGLE CRYSTALS

Distinct from 3D perovskites, 2D counterparts have anisotropic properties that are phase-dependent, and it is necessary to identify the unique structures and followed characteristics of each phase and tune the materials appropriately for targeted applications. From this point of view, selecting the organic ligands can be one of the main strategies. Variations of composition can influence dielectric properties, exciton binding energy, carrier transport properties, and bandgap energies. It is important to strategically select the appropriate composition and then synthesize the single crystals accordingly. Since single crystals have no grain boundaries with controlled crystal growth direction and low trap densities, they can be an ideal platform to not only analyze the intrinsic properties but directly use for applications. Synthesizing single crystals with high crystallinity and fewer defects can also be a direct way to enhance the performance in perovskite single crystal applications.

Typically, crystal structures of 2D perovskites can be classified with different phases depending on the organic ligands [Table 1]. As presented in Figure 2, (100)-oriented perovskites can be divided into three phases: RP, DJ, and ACI[22]. For the RP phase structure with $A'_2A_{n-1}B_nX_{3n+1}$, where monovalent ammonium cations (A') are used as large organic ligands. Due to no restriction in space, the monovalent spacer cation possesses significant flexibility for folding or disordering. As a result, an aliphatic or aromatic ammonium cation of almost any size can be accommodated by the spacer cation (A'). The RP phase shows (1/2,1/2) in-plane displacement along the ab-plane and a staggered configuration is also observed, and there is Van-der-Waals force between the monovalent cations [Table 1, Figure 2A]. Among these three phases, RP-phase perovskites have been investigated the most owing to their molecularly flat surface, ease of mechanical exfoliation, and lack of dangling bonds at the surface[10]. In the structure of the DJ phase, a general formula is $A'A_{n-1}B_nX_{3n+1}$ with a divalent ammonium spacer (A') that can bridge between two inorganic layers through a terminal hydrogen bond [Figure 2B]. The DJ phase in OIHP typically does not show any shift, which is (0,0) displacement, allowing it to stack perfectly. For these reasons, it can build a more stable crystal structure compared to the RP phase. The ACI phase can be explained into the structure that blends the RP phase's chemical composition combined with the DJ phase's structural characteristics, which has a formula of $A'A_nB_nX_{3n+1}$ and (1/2, 0) displacement along the b-axis[23]. In this phase, spacer cations (A') and small cations (A) are alternately placed along with the layers. This means small cations (A) are present within both the cage and the organic spacer layers [Figure 2C]. Variations of organic spacer cations (A') in 2D perovskites can change the distance between inorganic layers and determine quantum well structures with related characteristics of materials for device applications. In detail, depending on the species of spacer cations that include monovalent and divalent ammonium cations, the following respective type of bonding results in different bonding strengths and it can lead to variations in factors such as equatorial Pb-X-Pb bonding angles, adjacent X⋯X distances of the inorganic layers, and octahedral distortion. To regulate these factors in materials design, there are multiple crystallisation methods for 2D perovskites; however, most of DJ and ACI phases are synthesized with a cooling HX-based precursor method[4,24-28]. In addition, there are few studies on ACI phase perovskite single crystals. It is necessary to further develop and optimise the synthetic methods for DJ and ACI phases. In this section, the synthesis of single crystals will be investigated with phase-dependent strategies of 2D perovskite materials design.

HX-based precursor method

The formation of single crystals in a supersaturated solution can be described in two stages: nucleation and crystal growth. The crystal growth step can affect the quality of single crystals, corresponding to the solute diffusion and deposition rate on the crystal surface. Cooling HX-based precursors (hydrohalic acid, X = I, Br, Cl) is one of the commonly utilized strategies. For preparing the precursor solution, inorganic metal salt and organic materials are dissolved in aqueous HX solution typically mixed with hypophosphorous acid, and the temperature of the solution is increased to approximately higher than 100 °C until it becomes clear.

Table 1. (100)-oriented 2D OIHPs

| Phase	Formula	Bonding type	Displacement
Ruddlesden-Popper phase (RP)	$A'_2A_{n-1}B_nX_{3n+1}$ (A': monovalent)	Van-der-Waals force between organic spacers & Hydrogen bonds with inorganic layers	(1/2,1/2) displacement along the ab-plane
Dion-Jacobson phase (DJ)	$A'A_{n-1}B_nX_{3n+1}$ (A': divalent)	Hydrogen bonds only with inorganic layers	(0,0) displacement (eclipsed)
Alternating Cations in the Interlayer space phase (ACI)	$A'A_nB_nX_{3n+1}$ (A': monovalent)	Combination of Van-der-Waals force and Hydrogen bonds	(1/2,0) displacement along the b-axis
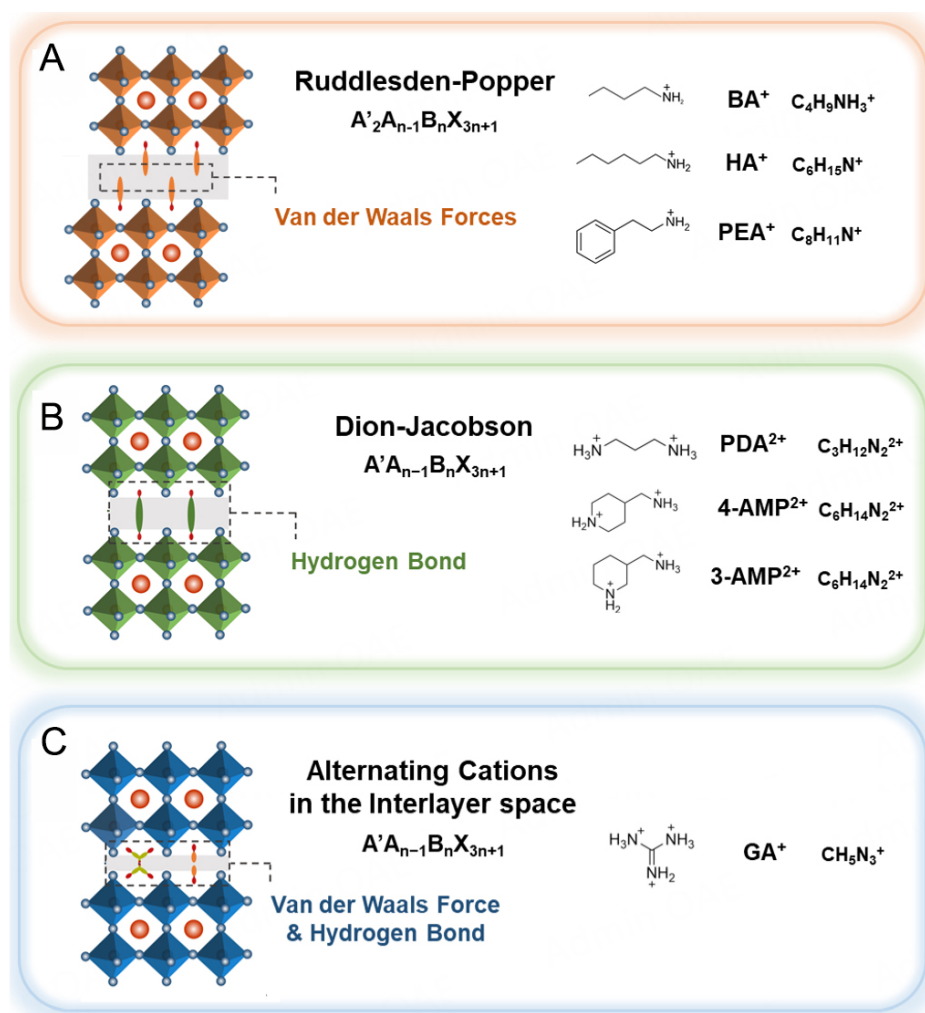
Figure 2. Classification of crystal structures for 2D OIHPs according to phases and organic ligands. (A-C) Structures and organic ligands of three types of (100) oriented 2D OIHPs; (A) Ruddlesden-Popper (RP), (B) Dion-Jacobson (DJ), and (C) Alternating cations in the interlayer space (ACI) phase. Reprinted with permission from ref.[22]: Copyright 2021, Wiley-VCH GmbH.

In the cooling down process, the solubility also diminishes and supersaturation causes the nucleation of single crystals as the temperature of the precursor decreases. Single crystals are obtained by gradually lowering from high temperature to room temperature, and cooling rate can influence the growth of single crystals. Controlling the cooling rate is crucial for producing large-sized single crystals with high quality by preventing multiple nucleation sites[29,30]. This HX-based precursor method can be used to synthesize all the phases [Figure 3]. Figure 3A is a representative schematic diagram that shows the growth of RP phase
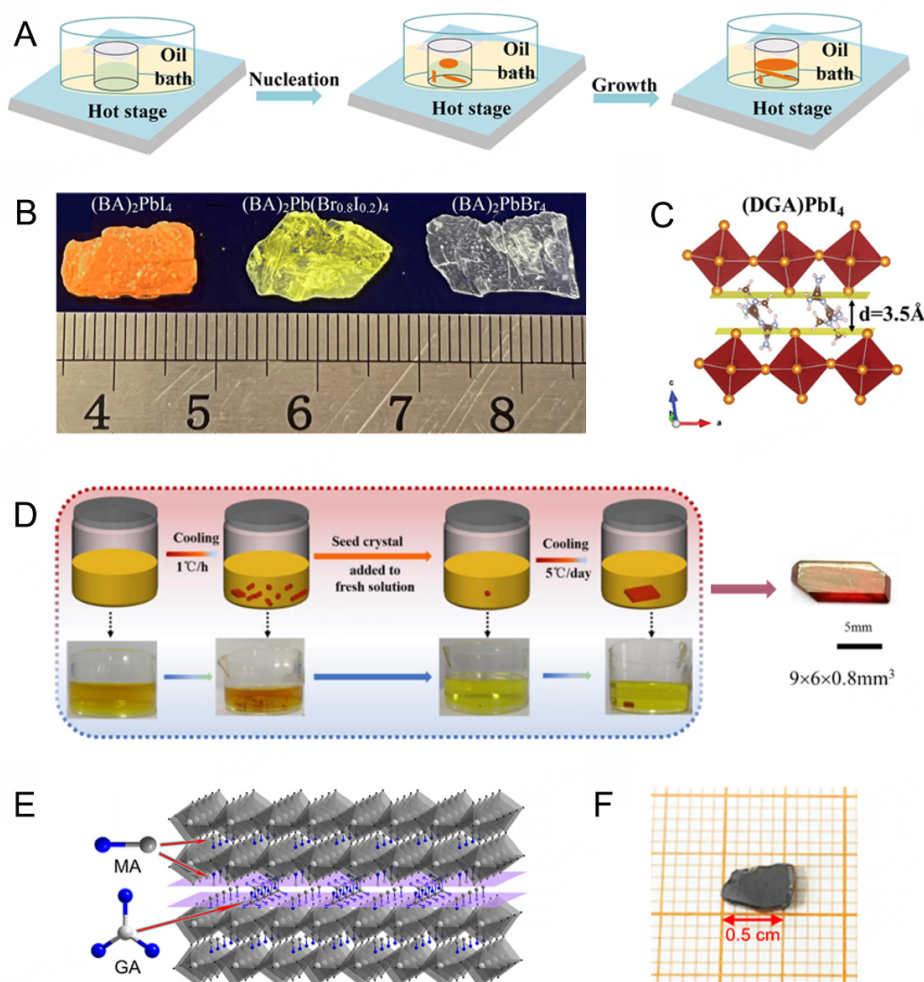
Figure 3. Crystallization of RP, DJ, and ACI phase 2D OIHP single crystals with cooling HX-based precursor method. (A) Schematic illustration of procedure to grow single crystals and (B) Optical image of RP phase $BA_2Pb(Br_xI_{1-x})_4$ single crystals. Reprinted with permission from ref.[31]: Copyright 2023, Royal Society of Chemistry. (C) Crystal structures of $(DGA)PbI_4$ and (D) Schematic and optical images of DJ phase DGA_2PbI_4 single crystals. Reprinted with permission from ref.[25]: Copyright 2022, Wiley-VCH GmbH. (E) 2D bilayered crystal structures and (F) Photographs of $GAMA_2Pb_2I_7$ single crystals. Reprinted with permission from ref.[27]: Copyright 2023, Elsevier.

$BA_2Pb(Br_xI_{1-x})_4$ single crystals in HX acid aqueous solutions, and different colors of plate-like centimeter-size $(BA)_2Pb(Br_xI_{1-x})_4$ single crystals grown in pure HI, HI + HBr, and pure HBr acids, respectively, are shown in Figure 3B[31]. In the process of DJ phase $(DGA)PbI_4$ single crystal growth, the seed-induced growth method was adopted to obtain high-quality large-sized single crystals [Figure 3C and D]. Concisely, to form seed crystals, the precursor was rapidly cooled down, and then the crystals were dissolved in a solvent to make a saturated solution. To get large $(DGA)PbI_4$ single crystals, a fresh seed crystal was put in the solution[25]. Figure 3E illustrates the ACI phase $(GA)(MA)_2Pb_2I_7$ structure, where hydrogen bonds bind the orderly arranged MA^+ and GA^+ organic cations to the bilayer perovskites. To crystallize this $(GA)(MA)_2Pb_2I_7$ perovskites, the precursor was mixed completely at 230 °C until there was no precipitation. As the precursor cooled, tiny $(GA)(MA)_2Pb_2I_7$ powder-like crystals appeared. The temperature was then gradually lowered from 65 °C to room temperature (1 °C /day) to allow the growth of millimeter-sized large crystals [Figure 3F][27]. In short, the temperature-lowering method with an HX-based solution is simple, convenient, and applicable for the growth of 2D perovskite single crystals containing DJ and ACI phases and the RP

phase [Table 2]. However, it is not suitable for low solubility materials at high temperatures.

Apart from this cooling down method, the space-confined method can also be selected for the crystallization of 2D single crystals with an HX-based precursor. In this approach, single crystals are grown between two substrates. This method is effective for preparing single-crystalline thin films while controlling their thickness. Using this method, millimetre-scale $BA_2MA_{n-1}Pb_nX_{3n+1}$ (n = 1~3) single crystal films were shown with nanometre thickness. By evaporating HI-based solution between two substrates at 80 °C, 2D perovskite single crystal membranes could be formed[32]. However, given that some flexible substrates are sensitive to acid, a synthetic method with the HX-based precursor is necessary to be further developed while maintaining the strength that can be applied to all 2D phases.

Organic solvent-based precursor method

There are various advanced methods involving organic solvents, including antisolvent vapor-assisted (AVC), space-confined, and surface tension-controlled techniques. The AVC method uses the diversity in solubility of perovskites across various solvents, which is also introduced for fast crystallization deposition in perovskite films. For single crystals, antisolvent diffuses in the precursor and antisolvent vapor with low solubility causes crystallization. The RP phase perovskites, such as PEA_2PbBr_4 and PEA_2PbI_4 single crystals, have been reported by the AVC method[33-35]. Recently, Zhang *et al.* suggested a new biphasic swimming top-down method in which long-chain alkane (n-$C_{12}H_{26}$) is utilized as the upper layer of the solution instead of an antisolvent, offering a flat liquid-liquid limiting confined interface and sufficient traction for 2D crystal growth[36]. RP phase $(BA)_2(MA)Pb_2I_7$ perovskites are crystallized by this new method as depicted in Figure 4A-C[36]. Since n-butylameine iodide ($C_4H_9NH_3I$, BAI) molecules have unique amphiphilic properties with a hydrophilic polar group ($-NH_3^+$) and a nonpolar alkyl chain hydrophobic group (C_4H_9), the alkyl-chain group ($-C_4H_9$) could preferentially dissolve in n-$C_{12}H_{26}$ but the $-NH_3^+$ group could dissolve in γ-butyrolactone (GBL). In this process, n-$C_{12}H_{26}$ is partially dissolved in the precursor solution and acts as an antisolvent by accelerating crystal nucleation with reducing saturation solubility. At the same time, GBL slowly diffuses into the air through the n-$C_{12}H_{26}$ layer. Therefore, the $(BA)_2MAPb_2I_7$ crystal seed preferentially nucleates at the interface of biphasic n-$C_{12}H_{26}$/GBL due to the preferential enrichment of $C_4H_9NH_3^+$ and I^- ions at the n-$C_{12}H_{26}$-GBL interface, and high-quality $(BA)_2MAPb_2I_7$ single crystals with few defects were successfully synthesized[36].

The space-confined method can be suggested as an efficient way of controlling the thickness of perovskite single crystals. Constrained spaces allow for flexible regulation of the thickness of perovskites. In addition, the size and crystal quality of these single crystal films are also important considerations. By applying proper techniques to the confined area, it can be a straightforward way to modify the thickness of perovskite crystal films, and a platform to optimize their size, quality, and design. Furthermore, with a nonwetting surface of substrates, the dragging force of solvent molecules decreases, allowing for extended transport of ions along the limited area in this approach. As the precursor is gradually cooled, RP phase $(BA)_2(MA)_2Pb_3I_{10}$ single crystals grow between the substrates and the nonwetting surface weakens the interaction between substrate and solvent, which can accelerate the transportation of solvents [Figure 4D][37]. Currently, Dong *et al.* have successfully obtained centimeter-sized high-quality DJ phase $(DPA)PbBr_4$ single crystals through a space-confined antisolvent-assisted crystallization method for the first time[38], indicating the possibility of broadening the synthesis methods of DJ and ACI phases.

Different from the space-confined method, the surface-tension method was suggested as a means for obtaining 2D perovskite single crystals because surface tension plays a part in the nucleation and growth of crystals. As depicted in Figure 4E, the Gibbs free energy change is positive on the surface ($\Delta G_{surface} > 0$) and

Table 2. (100)-oriented 2D OIHP single crystals

Phase	Composition		Initial temperature	Ref.
RP	$(BA)_2PbBr_4$	$n = 1$	100 °C	[3]
RP	$(BA)_2PbI_4$	$n = 1$	140 °C	[31]
RP	$(BA)_2PbBr_4$	$n = 1$	140 °C	[31]
RP	$(PEA)_2(MA)_{n-1}Pb_nI_{3n+1}$	$n = 1\text{-}3$	90 °C	[29]
RP	$(PMA)_2PbI_4$	$n = 1$	105 °C	[30]
DJ	$(3AP)PbCl_4$	$n = 1$	120 °C	[4]
DJ	$(3AP)PbBr_4$	$n = 1$	140 °C	[4]
DJ	$(3AP)PbI_4$	$n = 1$	180 °C	[4]
DJ	$(3\text{-}AMP)(MA)_{n-1}Pb_nI_{3n+1}$	$n = 1\text{-}4$	130 °C	[28]
DJ	$(4\text{-}AMP)(MA)_{n-1}Pb_nI_{3n+1}$	$n = 1\text{-}4$	130 °C	[28]
DJ	$(BDA)PbI_4$	$n = 1$	90 °C	[24]
DJ	$(DGA)PbI4$	$n = 1$	90 °C	[25]
DJ	$(3AMPY)(FA)Pb_2I_7$	$n = 2$	-	[26]
ACI	$(GA)(MA)_2Pb_2I_7$	$n = 2$	65 °C	[27]

negative in the bulk ($\Delta G_{bulk} < 0$), with r_0 representing the critical nucleus radius. The surface nucleation barrier is also lower than the bulk, favoring crystal nucleation and growth at the surface. Additionally, Figure 4F demonstrates that droplets with larger contact angles have lower nucleation barriers, allowing stable crystal growth ($r > r_0$), whereas those with smaller angles have higher nucleation barriers, making small nuclei ($r < r_0$) unstable and prone to degradation[39].

The 2D perovskites have been reported with various crystallization methods based on HX or organic solvent precursors. Although many methods exist for 2D perovskite single crystals with a single inorganic layer ($n = 1$), preparing single crystals with $n > 1$ remains a significant obstacle owing to the intricate balance of ionic species within the precursor solution. Phase-pure crystal formation is not easily controlled when the small perovskite cation and the large organic spacer are not equally soluble[40-42]. The process has a substantial variation depending on the precursors because the optimized parameters including concentration, molar ratio, and temperature should be experimentally set at all times, making the process described technically difficult. Even small deviations from optimal concentrations lead to impurities, resulting in crystals with thicker ($n + 1$) or thinner ($n - 1$) single crystals, and as the number of inorganic layers (n) increases, synthesis becomes even more challenging[43,44].

PHASE-DEPENDENT CHARACTERISTICS

As seen in Figure 2 and Table 1, there are three distinct types of 2D perovskites with unique structures. In the last chapter, 2D perovskite materials design strategies are suggested with the configuration of organic cation according to the phases and tuning inorganic layer thickness (n) within phases. These modifications in crystal structures result in variations of optical and charge transport properties; hence, in this chapter, these properties are developed depending on the types of 2D phases.

Ruddlesden-Popper (RP) phases

The organic cations in 3D perovskites are encapsulated within the inorganic octahedron, whereas 2D perovskites are structured with separated layers by inserting large organic cations. Depending on the 2D perovskite phases, types of organic spacers and following structures are different so that they can make differences in their properties. In the case of RP phase perovskites, there is less restriction in organic spacers, making them the most investigated among these three 2D phases. Figure 5A is a representative
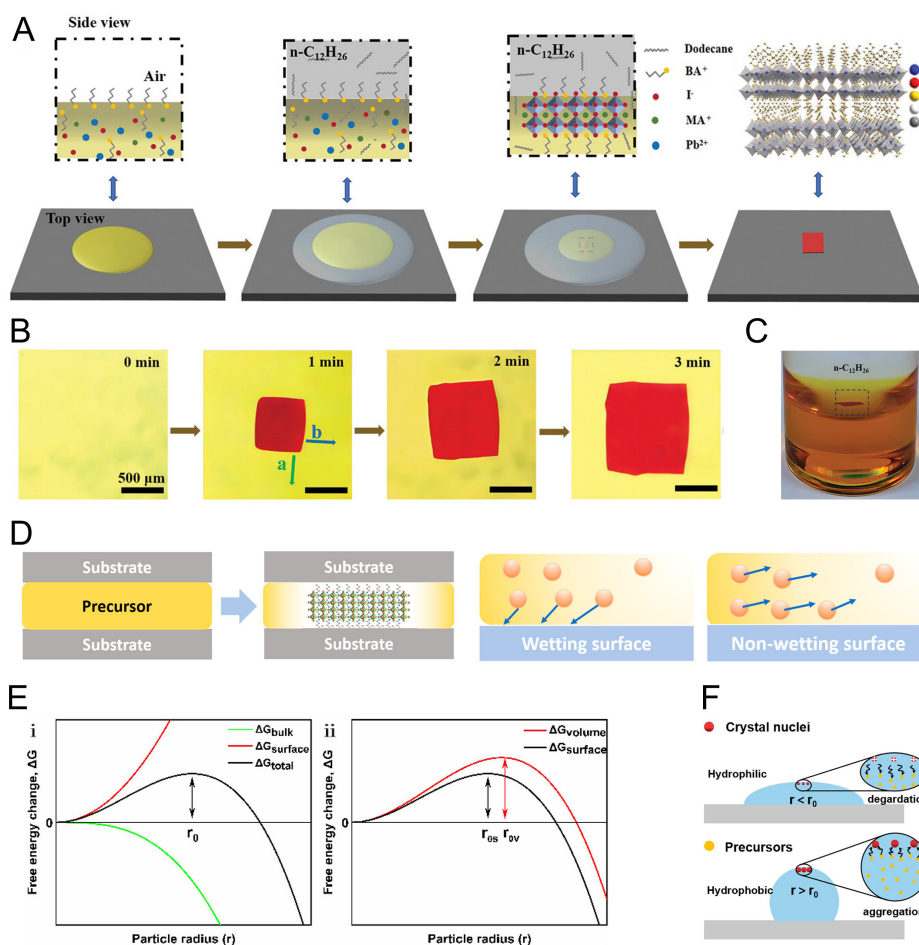
Figure 4. Various crystallization methods with organic solvent-based precursor. (A) Schematic crystal growth mechanism, (B) *In situ* growth process, and (C) An image of the $(BA)_2(MA)Pb_2I_7$ single crystals by swimming top-down growth. Reprinted with permission from ref.[36]: Copyright 2024, Wiley-VCH GmbH. (D) Schematic illustration of the space-confined method and the ion transportation on wetting and nonwetting surfaces for the growth of $(BA)_2(MA)_2Pb_3I_{10}$ single crystals. Reprinted with permission from ref.[37]: Copyright 2018, American Chemical Society. (E) Illustration of the free energy change ΔG_{total} with particle radius (left), and free energy change between volume and surface nucleation in precursor solution (right). (F) The schematic diagram of the floating growth mechanism of $(BA)_2(MA)_{n-1}Pb_nI_{3n+1}$ (n = 1-5) single crystals from droplets on hydrophilic and hydrophobic substrates. Reprinted with permission from ref.[39]: Copyright 2022, American Chemical Society.

X-ray diffraction (XRD) result of RP $(BA)_2(MA)_{n-1}Pb_nI_{3n+1}$ single crystals depending on the number of inorganic layers (n)[45]. As 2D perovskite layers thicken with the introduction of MA cations, the unit cell expands incrementally with each added layer. These changes can be tracked using XRD, which displays an additional low-angle reflection for each new layer. For example, the n = 2 structure shows two evenly spaced reflections and the n = 3 structure shows three reflections below 2θ = 14. $(C12)_2(MA)_{n-1}Pb_nI_{3n+1}$ single crystals also showed similar stacking peaks. Specifically, for crystals with n = 2, 3, 4, and 5, there are three, four, five, or six reflections below 2θ = 14, respectively[40]. As "n" increases, more peaks show up, implying the existence of more inorganic layers following the piled direction[39,41,45,46]. Aside from the thickness of inorganic layers, 2D perovskite single crystals showed distinguished plane-dependent properties. The top and side planes showed different XRD patterns [Figure 5B] and the scanning electron microscopy (SEM) images [Figure 5C and D][47]. Consistent with typical 2D layered structures, the SEM image of the (001) plane revealed a very smooth surface, but the (010) plane displayed a periodically layered image that showed neighboring layers connected through a weak van der Waals force.
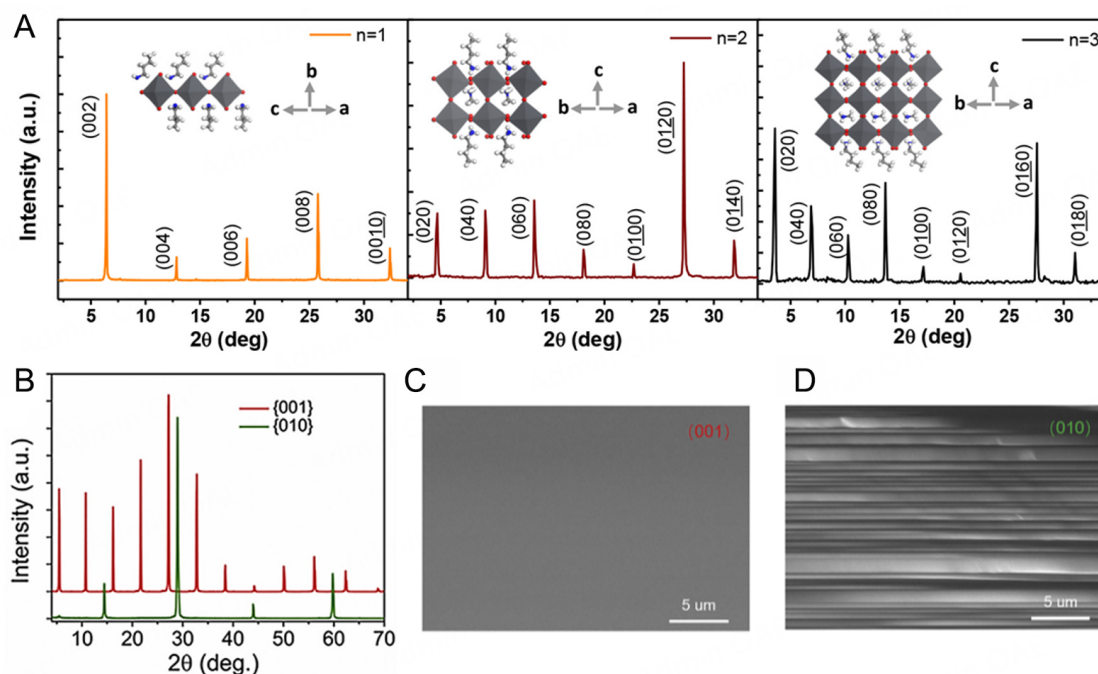
Figure 5. Structural properties of 2D RP phase perovskite single crystals. (A) XRD patterns of $(BA)_2(MA)_{n-1}Pb_nI_{3n+1}$ (with n = 1-4). Reprinted with permission from ref.[45]: Copyright 2018, American Chemical Society. (B) XRD patterns from (001) and (010) planes, and SEM images for (C) (001) and (D) (010) planes of PEA_2PbI_4 single crystals. Reprinted with permission from ref.[47]: Copyright 2019, Elsevier.

These distinct plane-dependent structural properties can induce anisotropic optical and carrier transport properties. Figure 6 shows a comparison of differences according to changes of inorganic layer thickness (n) and their exposed plane. The properties of bandgap tunability of 2D perovskites are demonstrated by the optical bandgaps from the absorption spectra in Figure 6A, which are 2.3, 2.1, 2.0, 1.9, and 1.8 eV from n = 1 to 5, respectively. Lower n values exhibit a strong excitonic impact, confirming the large exciton binding energy of 2D perovskites. This tendency is explained, as predicted, by the dielectric and quantum confinement effects of 2D perovskites. In the inherent quantum-well structure such as $(BA)_2(MA)_{n-1}Pb_nI_{3n+1}$ (n = 1-4), inorganic layers act as quantum wells between organic layers, hence enabling increased exciton binding energy and improving the quantum confinement effect. The value of n impacts the crystal structure and eventually, the band structure is modulated. The optical characteristics of $(BA)_2(MA)_{n-1}Pb_nI_{3n+1}$ (n = 1-5) are demonstrated using the PL and ultraviolet-visible (UV-Vis) spectrum. A progressive redshift exciton PL peak (λ_{ex} = 450 nm) is seen as the value of n increases, as illustrated in Figure 6B. This indicates the variety of optical characteristics present in this series. Figure 6C displays the time-resolved PL decay curves for the n = 1-4 thin films, which can be used to evaluate carrier recombination lifetimes. They have demonstrated a consistent increase with n-value [τ_{avg} = 154, 244, 277, and 336 ps (n = 1-4), respectively][48]. The crystal structure, which in turn controls the band structure, is directly influenced by the value of n. Figure 6D and E displays the PL peak and the decay curve at (001) and (010) planes with an excitation wavelength of 510 nm. Interestingly, the average carrier lifetime recorded along the (001) plane is 5.1 ns, whereas it is just 0.3 ns along the (010) plane. Because the organic cations serve as an insulating layer between the conductive inorganic slabs, they restrict charge transmission, which is why the lifetime is lower.

Dion-Jacobson (DJ) phases
In comparison with RP phases, DJ phases contain divalent cations with hydrogen bonding but not van der Waals force, which results in smaller interlayer distances. It leads to a more rigid structure and shortened
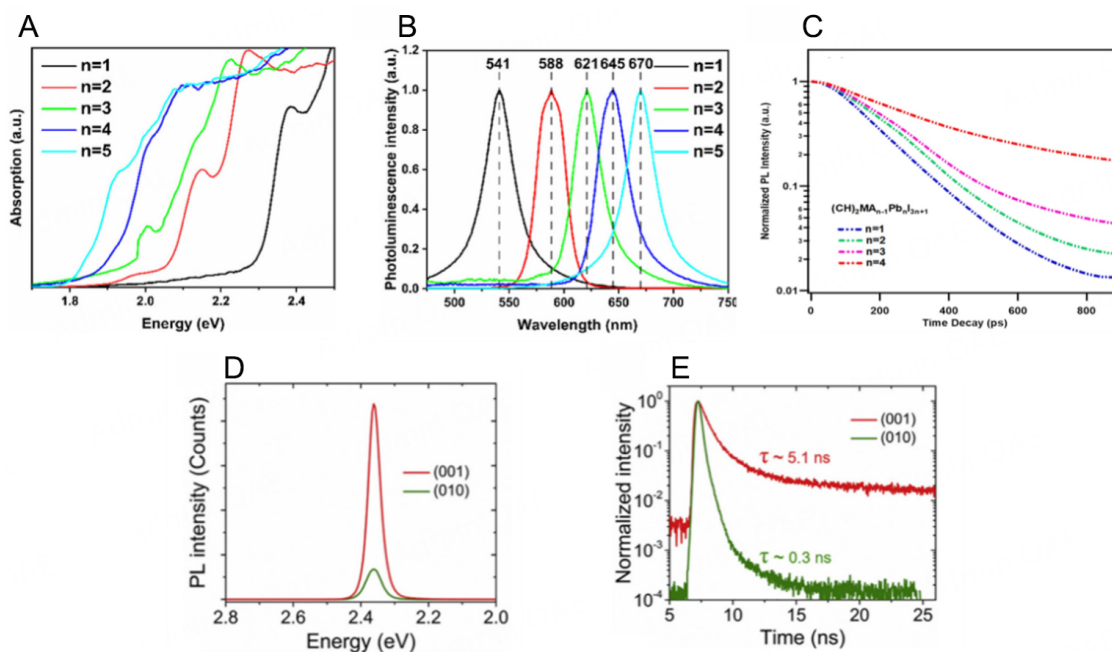
Figure 6. Optical properties of 2D RP phase perovskites. (A) Optical absorption and (B) photoluminescence (PL) spectrum (λ_{ex} = 450 nm) of $(BA)_2(MA)_{n-1}Pb_nI_{3n+1}$ (n = 1-5) single crystals. Reprinted with permission from ref.[39]: Copyright 2022, American Chemical Society. (C) Time-resolved PL (TRPL) decay profiles (λ_{ex} = 401 nm) of $(CH)_2(MA)_{n-1}Pb_nI_{3n+1}$ (n = 1-4). Reprinted with permission from ref.[48]: Copyright 2022, Springer Nature. (D) PL and (E) time-resolved PL (TRPL) spectra of (001) and (010) planes on $(PEA)_2PbI_4$ single crystals. Reprinted with permission from ref.[47]: Copyright 2019, Elsevier.

smaller I⋯I interlayer distances. Figure 7 presents a comparison of the differences based on modifications in the thickness (n) of the inorganic layer and its exposed plane. Figure 7A shows powder XRD (PXRD) results of $(mPDA)(MA)_{n-1}Pb_nI_{3n+1}$ single crystals depending on the number of inorganic layers (n). Similar to RP phases, as inorganic layers increase with the MA cations, the unit cell expands incrementally in DJ phases. It can be shown in an additional low-angle reflection following each added layer. The absorption and PL spectra of the DJ $(mPDA)(MA)_{n-1}Pb_nI_{3n+1}$ (n = 1-3) are exhibited in Figure 7B and C. With rising n, Pb-I-Pb angles increase and I⋯I interlayer distances decrease, hence influencing the bandgap energy drop[49]. Figure 7D and E presents the optical properties of DJ phases with diverse lengths of organic cations. DJ perovskites based on 1.3-propanediamine (PDA) and 1.4-butanediamine (BDA), which have relatively shorter spacers, show similar optical properties to 3D MAPbI₃ perovskites, while additional peaks are observed in 1.5-pentamethylenediamine (PeDA) (at 610 and 640 nm) and 1.6-hexamethylenediamine (HDA) (at 590 nm)-based perovskites. These additional exciton peaks do not appear clearly in PDA and BDA because, compared to long-chain spacers, the short-chain spacers lessen the distortion of the DJ perovskite. DJ perovskites with longer spacers exhibited shorter exciton lifetimes owing to thicker quantum well barriers of 81 and 64 ns in PeDA and HAD perovskites, respectively, than those of 84 and 96 ns in the PDA and BDA perovskites with thin barriers [Figure 7F][50-52].

There are three types of structural contributions in 2D perovskites, which include the bonding types of organic spacers, the equatorial Pb-I-Pb bonding angles, and the adjacent I⋯I distances of the inorganic layers. As depicted in Figure 8A, DJ phases consist of divalent organic cations that form eclipsed arrangements of successive inorganic layers without relative displacements[53]. These divalent organic cations contain two amino groups at both terminal positions which interact with adjacent inorganic frameworks through hydrogen bonding. Compared to RP phases, DJ phases remove the van der Waals gap
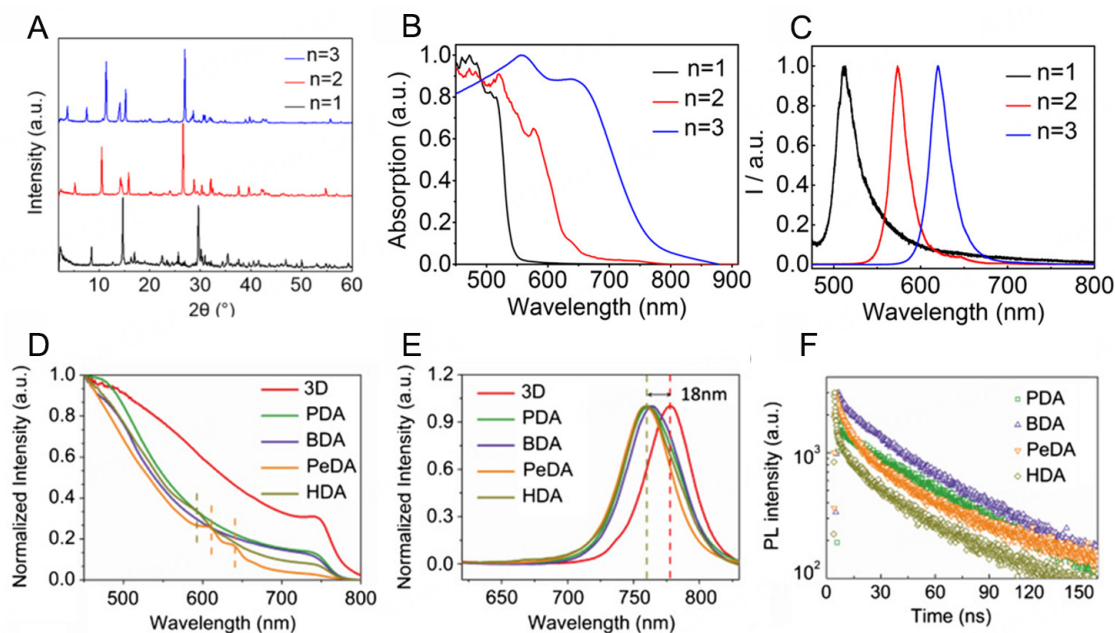
Figure 7. Structures and optical properties of 2D DJ phase perovskites. (A) XRD patterns of $(mPDA)(MA)_{n-1}Pb_nI_{3n+1}$ (with n = 1-3), (B) optical absorption, and (C) PL spectrum (λ_{ex} = 510 nm) of $(mPDA)(MA)_{n-1}Pb_nI_{3n+1}$ (n = 1-3) single crystals. Reprinted with permission from ref.[49]: Copyright 2021, American Chemical Society. (D) Optical absorption, (E) PL, and (F) TRPL spectra of PDA, BDA, PeDA, and HAD-based DJ perovskites compared to 3D $MAPbI_3$ perovskites. Reprinted with permission from ref.[50]: Copyright 2019, Wiley-VCH GmbH.

by forming hydrogen bonds resulting in a more durable framework and shortened I···I interlayer distances. The small adjacent I···I distances can influence band structure and charge dynamics[54]. Vasileiadou *et al.* reported that DJ perovskites have higher distortions in Pb-I-Pb bonding angle than RP perovskites, while they have noticeably smaller neighboring interlayer I···I distances[55]. Comparing DJ perovskites of $(3AMP)(MA)_{n-1}Pb_nI_{3n+1}$ and $(4AMP)(MA)_{n-1}Pb_nI_{3n+1}$ (n = 2-4) with RP perovskites of $(BA)_2(MA)_{n-1}Pb_nI_{3n+1}$, $(PA)_2(MA)_{n-1}Pb_nI_{3n+1}$, and $(HA)_2(MA)_{n-1}Pb_nI_{3n+1}$ (n = 2-4), DJ perovskites have larger Pb-I-Pb equatorial angles, considerably lesser I···I interlayer distances, and lower octahedral distortions. Additionally, they have narrower bandgaps and PL values due to the combined structural impact of medial angular distortions and small I···I interlayer distances [Figure 8B and C][55]. Li *et al.* synthesized RP and DJ perovskite single crystals from the same organic amine and compared optoelectrical properties between RP and DJ phases[56]. As shown in Figure 8D, DJ $(4AEPy)PbI_4$ perovskites show a lower bandgap due to the closer distances between successive inorganic layers and the larger Pb-I-Pb angle. Corresponding to the band edges of absorption, PL emission peaks of RP $(4AEPy)_2PbI_4$ and DJ $(4AEPy)PbI_4$ are 527 and 571 nm, respectively [Figure 8E]. The PL intensity of RP perovskites is significantly stronger than that of DJ perovskites since the exciton produced in the RP perovskites has more significant radiation recombination and DJ $(4AEPy)PbI_4$ shows more p-type electronic properties than RP $(4AEPy)_2PbI_4$, which will be more contributing to charge injection. Figure 8F shows photocurrent signals on 455 nm light. The photocurrent of DJ $(4AEPy)PbI_4$ is four times higher than that of RP $(4AEPy)_2PbI_4$ which can be attributed to the larger exciton binding energy of RP phases[56].

The bandgap and electrical characteristics of halide perovskites are directly influenced by the Pb-X-Pb equatorial angles, as previously stated. These angles are significant in determining the properties of the material, which can result in defects that restrict carrier mobility[57,58]. Additionally, the closer and more uniform inorganic layer stacks of DJ perovskites reduce the barrier to charge transfer between the inorganic octahedrons, improving charge transport in optoelectronic devices[59].
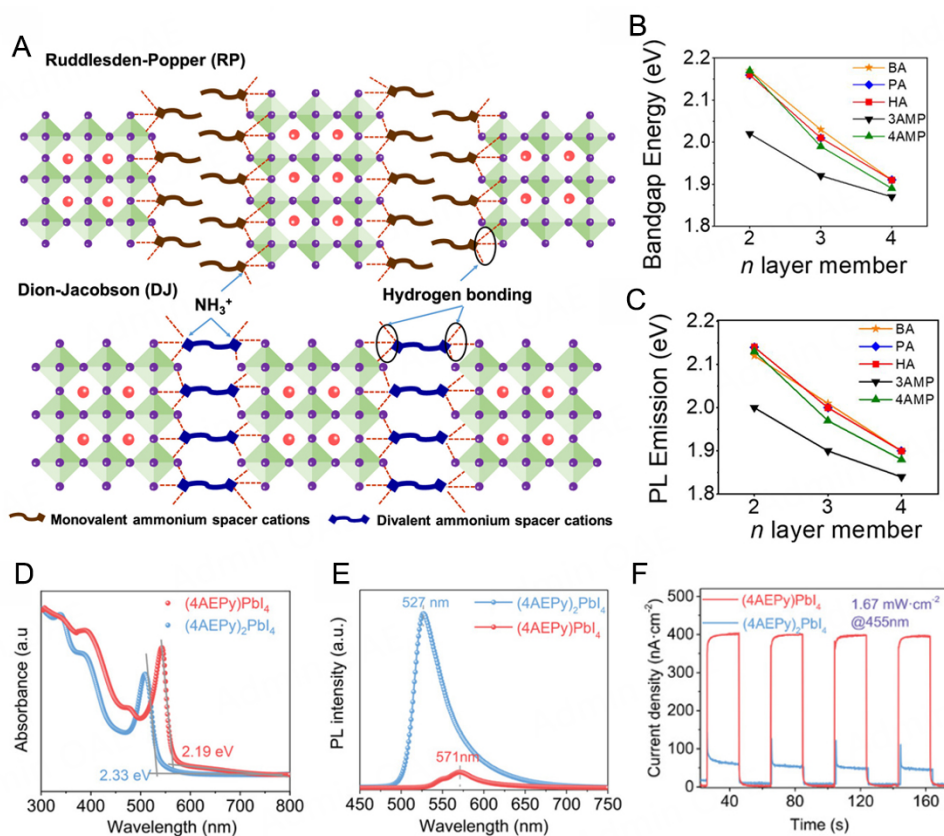
Figure 8. Comparison of structure and optoelectrical properties between RP and DJ phases. (A) Crystal structures of RP and DJ phase perovskites (n = 3). Reprinted with permission from ref.[53]: Copyright 2019, American Chemical Society. (B) Bandgap and (C) PL emission value depending on inorganic layer thickness (n) of $(BA)_2(MA)_{n-1}Pb_nI_{3n+1}$, $(PA)_2(MA)_{n-1}Pb_nI_{3n+1}$, $(HA)_2(MA)_{n-1}Pb_nI_{3n+1}$, $(3AMP)(MA)_{n-1}Pb_nI_{3n+1}$, and $(4AMP)(MA)_{n-1}Pb_nI_{3n+1}$. Reprinted with permission from ref.[55]: Copyright 2021, American Chemical Society. (D) Absorption, (E) PL, and (F) photocurrent at 455 nm light source of $(4AEPy)_2PbI_4$ and $(4AEPy)PbI_4$ perovskites. Reprinted with permission from ref.[56]: Copyright 2023, Wiley-VCH GmbH.

Alternating cation in interlayer space (ACI) phases

In the ACI phase, long spacer organic cations and small organic cations are placed alternately in the interlayer space. The higher crystal symmetry and the introduction of MA cation in the spacer layer lead to a bandgap decrease than in the RP phases. Lower dielectric confinement of these quantum well structures in ACI phases causes a lower exciton binding energy. Figure 9A and B represents SEM images of ACI phase perovskite single crystals, which are $(GA)(MA)_nPb_nI_{3n+1}$ (n = 1-3) crystals and $(BEA)_{0.5}MA_3Pb_3I_{10}$ crystals showing a plate-like crystal morphology, respectively. These plates are irregular parallelepipeds growing preferentially along one dimension. In the case of $(GA)(MA)_nPb_nI_{3n+1}$ (n = 1-3) crystals, red needles (n = 1, ACI1), dark red needles (n = 2, ACI2), and black needles (n = 3, ACI3) were obtained[23]. As shown in Figure 9C, the XRD pattern of $(GA)(MA)_2Pb_2I_7$ single crystal presents repeated diffraction peaks at the (101) plane group. On the other hand, compared with the RP and DJ phases, the ACI phase shows distinguished trends in charge carrier dynamics. Similar to RP and DJ phases, the PL spectra of ACI phases exhibit a redshift with increasing layer thickness [Figure 9D], while PL decay time gets shorter as the number of layers decreases in contrast to other phases [Figure 9E]. Ghosh *et al.* interpreted these phenomena in ACI phases with exciton dynamics including free exciton recombination (FE) and self-trapping of the excitons (STE)[60]. As the number of inorganic layers increases, multiple exciton recombination predominates over
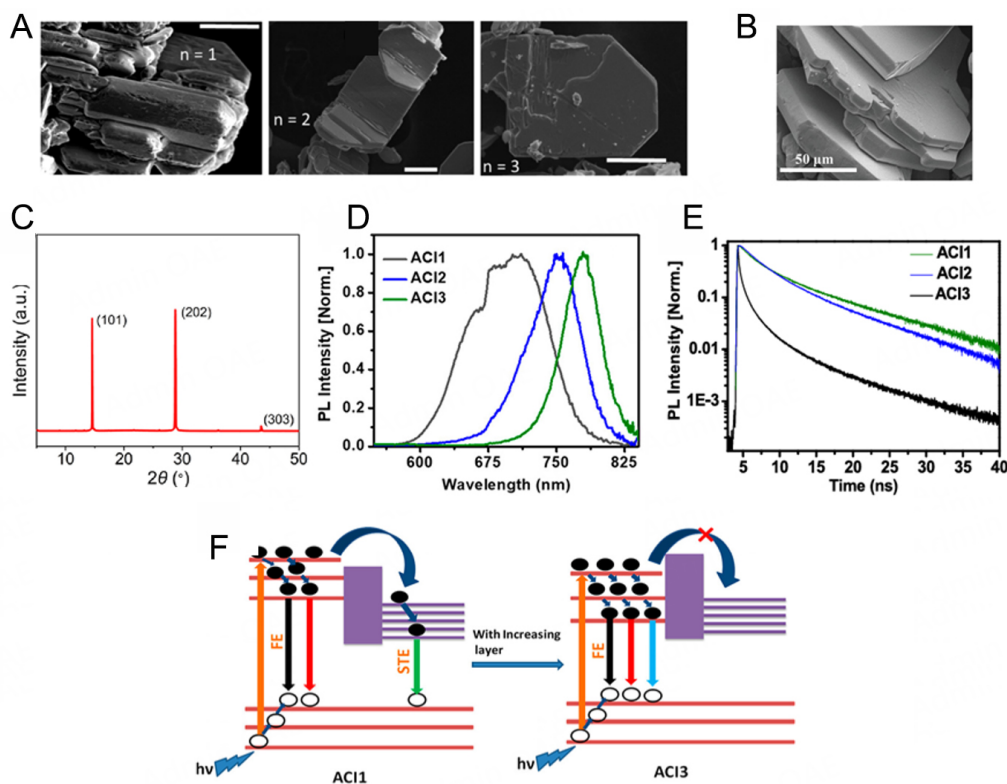
Figure 9. Morphologies and optical properties of 2D alternating cations in the interlayer space (ACI) phase perovskite single crystals. SEM images of (A) $(GA)(MA)_nPb_nI_{3n+1}$ (n = 1-3) and (B) $(BEA)_{0.5}MA_3Pb_3I_{10}$ crystals. Reprinted with permission from ref.[23,61]: Copyright 2017, American Chemical Society; Copyright 2019, Wiley-VCH GmbH. (C) XRD result of the $(GA)(MA)_2Pb_2I_7$ single crystal. Reprinted with permission from ref.[27]: Copyright 2023, Elsevier. (D) PL and (E) TRPL spectra of $(GA)(MA)_nPb_nI_{3n+1}$ (n = 1-3); ACI1 (n = 1), ACI2 (n = 2), and ACI3 (n = 3) perovskites, and (F) schematic illustration of exciton dynamics in ACI phases. Reprinted with permission from ref.[60]: Copyright 2021, American Chemical Society.

STE due to a considerably rapid STE, which is caused by a decreased bandgap and increased barrier height for the higher number of layers (n) [Figure 9F]. In short, ACI3 primarily includes FE, while ACI1 includes STE and FE.

In ACI phase structures, hydrogen bonding and van der Waals forces exist together. The hydrogen bonds between BEA^{2+} and $[PbI_6]^{4-}$ are stronger than Van der Waals force of RP phases, which can enhance the structural stability and light absorption as depicted in Figure 10A. The 3D $MAPbI_3$ with the less distorted crystal structure shows the narrowest bandgap, and the bandgap energy lessens with increasing the number of inorganic layers (n) in 2D ACI phases. Figure 10B illustrates the absorption edges and the bandgap reduction effect of the ACI, RP, and (110)-sliced perovskites (n = 1). Compared to RP phases which are distorted in both directions in the ab-plane, the ACI phases are distorted solely in one direction and exhibit higher symmetry and lower bandgaps. Owing to the greater distortion and the dihedral angle dependency caused by the (110) split of the perovskites, the most distorted arrangement of the (110)-sliced $(GA)_2PbI_4$ perovskite shows the largest bandgap[61,62]. Figure 10C presents the comparison of PL emissions between RP and ACI phase perovskites (n = 1-3). ACI $(BEA)_{0.5}(MA)_nPb_nI_{3n+1}$ shows higher PL intensity than RP $(BA)_2MA_{n-1}Pb_nI_{3n+1}$ series due to less distortion, shorter interlayer distance, and weak dielectric properties. It can be connected to the lower exciton binding energy of $(BEA)_{0.5}(MA)_nPb_nI_{3n+1}$ than $(BA)_2(MA)_{n-1}Pb_nI_{3n+1}$, which leads to the benefit of dissociating photogenerated carriers.
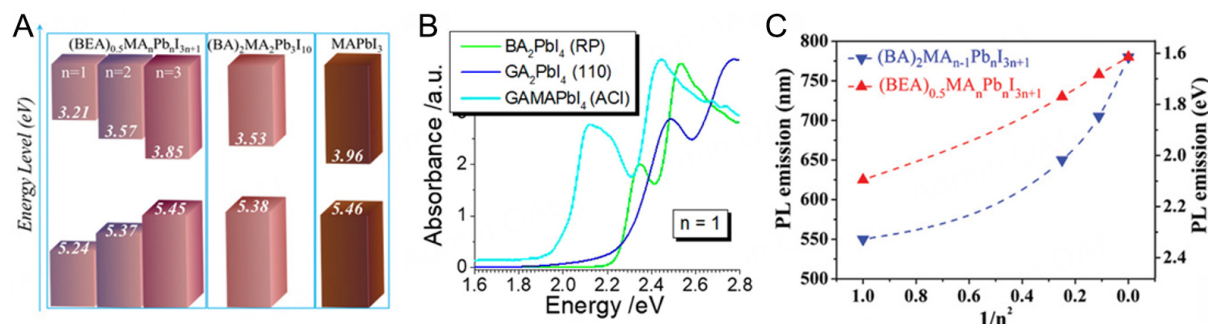
Figure 10. Comparison of structure and optoelectrical properties between RP and DJ phases. (A) Band energy diagram of 3D MAPbI$_3$, 2D RP (BA)$_2$(MA)$_2$Pb$_3$I$_{10}$ and ACI (BEA)$_{0.5}$(MA)$_n$Pb$_n$I$_{3n+1}$ (n = 1-3) perovskites. (B) Optical absorption spectra of RP (BA)$_2$PbI$_4$, (110)-cleaved (GA)$_2$PbI$_4$ and ACI (GA)(MA)PbI$_4$ perovskites. Reprinted with permission from ref.[23]: Copyright 2017, American Chemical Society. (C) Graphical representation of the (BEA)$_{0.5}$(MA)$_n$Pb$_n$I$_{3n+1}$ and (BA)$_2$(MA)$_{n-1}$Pb$_n$I$_{3n+1}$ series (n = 1-3). Reprinted with permission from ref.[61]: Copyright 2019, Wiley-VCH GmbH.

In summary, DJ phases are characterized by divalent organic cations that create eclipsed arrangements of consecutive inorganic layers without any relative displacement. These cations feature two amino groups at their ends, which form hydrogen bonds with nearby inorganic frameworks. Compared to RP phases, DJ phases eliminate the van der Waals gap by establishing hydrogen bonds, resulting in a more resilient framework and decreased I⋯I interlayer distances. The reduced distances between adjacent I atoms can significantly affect the band structure and charge dynamics. DJ phases display larger equatorial angles for Pb-I-Pb, significantly reduced I⋯I distances, and lower octahedral distortions. Additionally, the lower bandgap in DJ perovskites arises from the closer spacing between successive inorganic layers and the larger Pb-I-Pb angles. Furthermore, the closer and more uniform arrangement of inorganic layers in DJ perovskites can reduce the charge transfer barrier between inorganic octahedrons, thereby enhancing charge transport in optoelectronic devices. In ACI phase structures, hydrogen bonding and van der Waals forces coexist. The hydrogen bonds are stronger than the van der Waals forces present in RP phases, contributing to enhanced structural stability and improved light absorption. Unlike RP phases, which exhibit distortions in both directions within the ab-plane, ACI phases are distorted in only one direction, resulting in higher symmetry and lower bandgaps. In addition, the ACI phase displays greater PL intensity compared to the RP phase, attributed to reduced distortion, shorter interlayer distances, and weaker dielectric properties. Consequently, these structural factors should be considered when designing 2D perovskites for specific applications.

OPTOELECTRONIC APPLICATIONS

Much attention has been paid to 2D perovskites in recent years due to their enhanced stability, less ion migration, tuneable band structures, and flexible composition engineering. Compared to their polycrystalline films and 3D counterparts, 2D perovskites single crystals play essential roles in not only the fundamental study of intrinsic characteristics but high performance in optoelectronic applications such as photodetectors and X-ray detectors, owing to their low dark current, high sensitivity, and better stability with low trap density. In this section, we are focusing on applications for photodetectors and X-ray detectors of RP, DJ, and ACI phase single crystals.

Photodetectors

RP phase perovskites with monovalent organic spacers have garnered the most attention among 2D phases because they are easy to mechanically exfoliate and have high controllability in phase arrangement due to unconstrained space. Recently, we reported the lateral structure device of Au/(BA)$_2$PbBr$_4$ single crystal/Au as a photodetector and tested it as shown in Figure 11A. The device had the maximum photocurrent
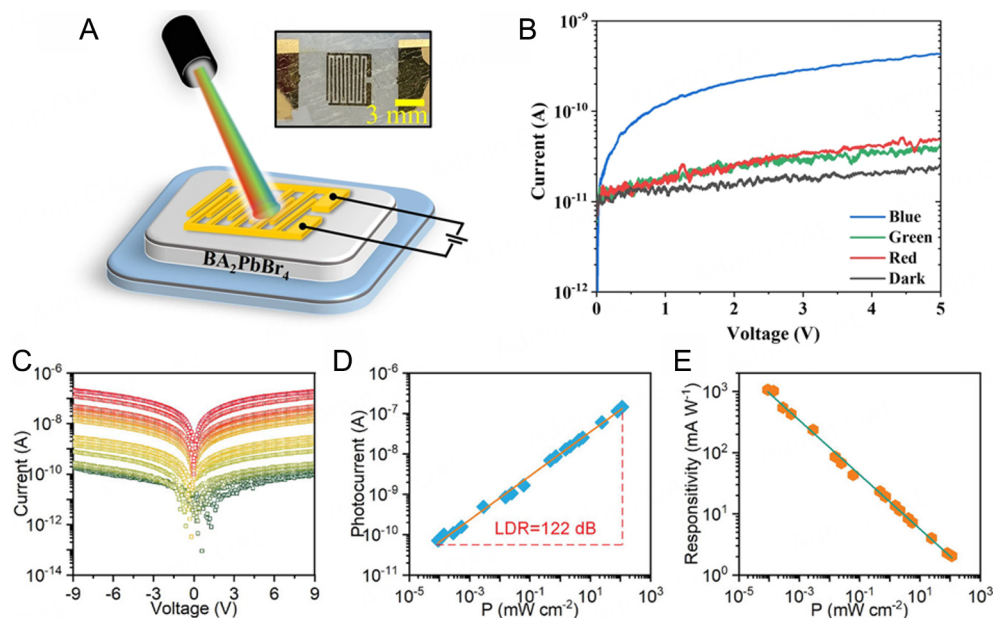
Figure 11. Performance of $(BA)_2PbBr_4$ single crystal-based photodetectors. (A) Schematic illustration and optical image and (B) current-voltage curves in the dark and under red, green, and blue light (634, 515, and 447 nm, respectively) of $(BA)_2PbBr_4$ photodetector. Reprinted with permission from ref.[3]: Copyright 2022, Springer Nature. (C) I-V curves in the dark and different power densities from 9×10^{-5} to 113 mW/cm², and relationship between (D) photocurrent and (E) responsivity at a 5 V bias. Reprinted with permission from ref.[63]: Copyright 2023, Wiley-VCH GmbH.

response when illuminated with blue light, and it also responded similarly to red and green light [Figure 11B]. Since fewer carriers can be stimulated to the sub-bandgap states, the gap in performance under various wavelengths grows greater at higher light intensities, suggesting that charge recombination affects performance more under red and green light. The maximum responsivity (R) and detectivity (D*) were obtained at 0.38 mA/W and 9.0×10^{10} Jones, respectively, with 0.5 µW/cm² of 447 nm light at 5 V bias. These findings point to the significant potential of $(BA)_2PbBr_4$ single crystal photodetectors, with a broad detection range that reaches the below bandgap region[3]. Gao *et al.* also studied BA_2PbBr_4 single crystals for UV photodetectors[63]. The I-V curves at dark and 375 nm light ranging of power densities from 9×10^{-5} to 113 mW/cm² are displayed in Figure 11C. Higher photocurrent can be shown at large voltage and power densities. A low dark current of 10-11 A was attained at 100 V/mm, which is significantly less than that of 3D perovskite-based photodetectors[64-67]. Suppression of ion migration in 2D perovskites and the exceptional quality of the $(BA)_2PbBr_4$ single crystal are the contributing factors to the low dark current. In addition, linear dynamic range (LDR) was calculated to be 122 dB, which is comparable to other 2D perovskite single crystal-based photodetectors[39], and the responsivity could reach 1,069 mA/W at 9.1×10^{-5} mW/cm² [Figure 11D and E].

Liu *et al.* also successfully prepared high-quality inch-sized 2D RP $(PEA)_2PbI_4$ single crystals with low trap density and showed anisotropy-dependent performances[47]. The planar-type photodetectors on (001) planes exhibit a significantly greater photoresponse compared to their counterparts on the (010) planes of the $(PEA)_2PbI_4$ single crystals. Figure 12A and B displays the device structures of the (001) and (010) planes, and I-V curves of the devices fabricated on the (010) planes are shown in Figure 12C under the identical light condition. The photocurrent of twenty devices fabricated on the (001) plane is obtained to be $4,552 \pm 65.6$ nA, but the devices with the (010) plane have a photocurrent of just 79 ± 3.4 nA at the same light intensity as illustrated in Figure 12D. Compared to counterpart photodetectors on the (010) plane, the
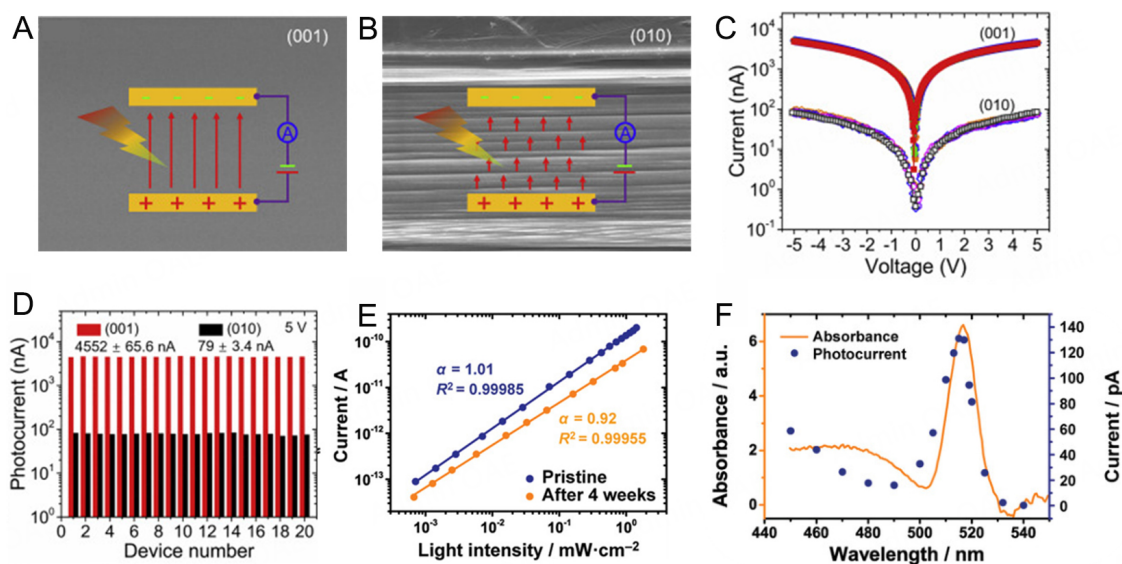
Figure 12. Photodetector structures fabricated on the (A) (001) and (B) (010) planes of a 2D (PEA)$_2$PbI$_4$ single crystals. (C) Current-voltage (I-V) curves of the devices fabricated on (001) plane and (010) plane under identical light conditions. (D) Photocurrent for twenty devices on (001) and (010) planes of the (PEA)$_2$PbI$_4$ single crystals. Reprinted with permission from ref.[47]: Copyright 2019, Elsevier. (E) (PEA)$_2$PbI$_4$ stability in the ambient environment. (F) Light absorbance spectrum and photoresponse of (PEA)$_2$PbI$_4$ under 0.28 mW cm^{-2} monochromatic light ranging from 450 to 540 nm of wavelength at 1 V. Reprinted with permission from ref.[69]: Copyright 2020, Wiley-VCH GmbH.

(001) plane appears to have 5,762% greater response. The 2D layered structure and the dielectric difference between the inorganic and organic layers in the (010) plane result in tightly bound excitons with low mobility[68]. Tu *et al.* also fabricated ultrathin PEA$_2$PbI$_4$ single crystal layers for narrowband photodetectors, about 33 nm containing 20 (PEA)$_2$PbI$_4$ monolayers[69]. After four weeks of storage in the ambient environment, PEA$_2$PbI$_4$ still exhibited a strong linear photoresponse, as shown in Figure 12E. Nonetheless, there is a restricted van der Waals interaction; oxygen and water molecules may permeate from the layer edges and degrade the ultrathin layer of PEA$_2$PbI$_4$ over a long period of storage under the ambient condition, resulting in a 70% reduction in responsivity. In addition, as illustrated in Figure 12F, the ultrathin PEA$_2$PbI$_4$ device shows a good match between the light absorption and photocurrent, presenting a clear peak at 517 nm.

As seen in Figure 12F, 2D RP phase thin layers can generate high narrowband excitonic light absorption, which can be promising candidates for filterless narrowband photodetectors[70,71]. However, in the case of RP phases, van der Waals forces enable the two large spacer cations to interact with one another and hydrogen bonds between two layers of organic cations and the inorganic layers. Because of this, even though RP perovskites show much better stability in a variety of conditions, the charge transport over the organic interlayers is impeded by a van der Waals gap between the layers. DJ perovskites formed by adding diammonium cations can decrease the interlayer spacing, remove the van der Waals gap, and improve structural stability, which brings benefits such as reduced ion migration and diminished quantum confinement effect. Significantly, enhanced lattice durability and a shorter interlayer spacing of DJ perovskites can promote effective charge carrier transport. Xiang *et al.* fabricated planar-type photodetectors on DJ (BDA)PbI$_4$ single crystals with interdigitated electrodes with a 22 μm spacing between adjacent electrodes [Figure 13A][72]. The I-V curves of the (BDA)PbI$_4$ single crystal photodetector, obtained with a laser of 462 nm and -10 to 10 V biases, are displayed in Figure 13B. The measurements were taken both in the dark and under illumination intensity. It is clear that the photocurrent increases in response to
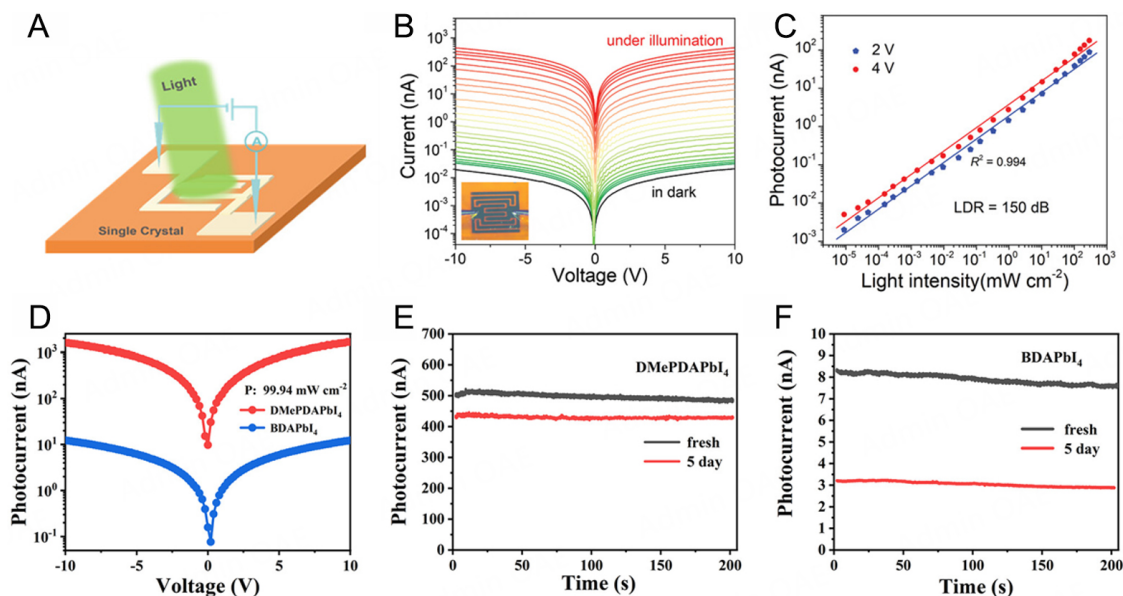
Figure 13. (A) Schematic diagram of 2D DJ perovskite single crystal photodetector. (B) I-V curves of the (BDA)PbI$_4$ single crystal photodetector under the dark and 462 nm illumination with intensities from 8.8×10^{-6} to 288.2 mW cm^{-2}. (C) Linear dynamic range (LDR) of the device measured at 2 and 4 V biases. Reprinted with permission from ref.[73]: Copyright 2020, Wiley-VCH GmbH. (D) Current-voltage (I-V) curves of the (DMePDA)PbI$_4$ (red) and (BDA)PbI$_4$ (blue) devices under identical light conditions at 532 nm. Photocurrent response stability for the (E) (DMePDA)PbI$_4$ and (F) (BDA)PbI$_4$ single crystal detector under identical conditions in ambient air. Reprinted with permission from ref.[72]: Copyright 2024, American Chemical Society.

an increase in driving voltage and illumination intensity. In practical applications, the low dark current helps signal-to-noise ratio rise, which is crucial for weak light detection. As displayed in Figure 13C, the photocurrent has a great linear response from 8.8×10^{-6} to 288.2 mW/cm^2. The response's nearly perfect linearity is indicated by the high correlation coefficient (0.994), which is extremely close to 1[73]. The (BDA)PbI$_4$ PSC photodetector has a higher LDR than previous planar-type RP perovskite photodetectors, which is calculated to reach up to 150 dB[47]. Recently, DJ (DMePDA)PbI$_4$ single crystals have been newly fabricated for photodetectors with high performances. As shown in Figure 13D-F, the photocurrent of the (DMePDA)PbI$_4$ is more than 100 times larger than that of the (BDA)PbI$_4$ with a 99.9 mW cm^{-2} illumination. Compared to (BDA)PbI$_4$, (DMePDA)PbI$_4$ has a larger Pb-I-Pb bond angle, a narrower bandgap, and a lower effective mass of electrons and holes. Furthermore, the organic cations in (DMePDA)PbI$_4$ displayed a higher energy of density of states (DOSs) than (BDA)PbI$_4$, suggesting a diminished interaction and weaker hydrogen bonding between the organic cations and inorganic layer. This reduces the energy barrier for out-of-plane charge transport. As a result, (DMePDA)PbI$_4$ has a greater detectivity of 2.50×10^{10} Jones and the photoresponsivity of18.04 mA/W than those of the(BDA)PbI$_4$ with 5.27×10^8 Jones and 0.15 mA/W, respectively. Additionally, under typical ambient circumstances without encapsulation, the photocurrent degradation of the (DMePDA)PbI$_4$ (11.5% degradation) in a long-term stability test is significantly lower than that of the (BDA)PbI$_4$ (57% degradation)[72]. These studies offer a wide range of possibilities for DJ perovskite single crystal design in the future.

ACI phase perovskite single crystals also have been demonstrated in applications for photodetectors. Figure 14A and B shows a (GA)(MA)$_2$Pb$_2$I$_7$ imaging sensor connected with an analyzer that records the spatially resolved photocurrent. The strong stability and light sensitivity of the imaging system were demonstrated by the ability to recover a high-resolution dolphin image from the photocurrent signal that was collected [Figure 14C]. In Figure 14D-F, the current exhibits consistent on-off switching behaviors with
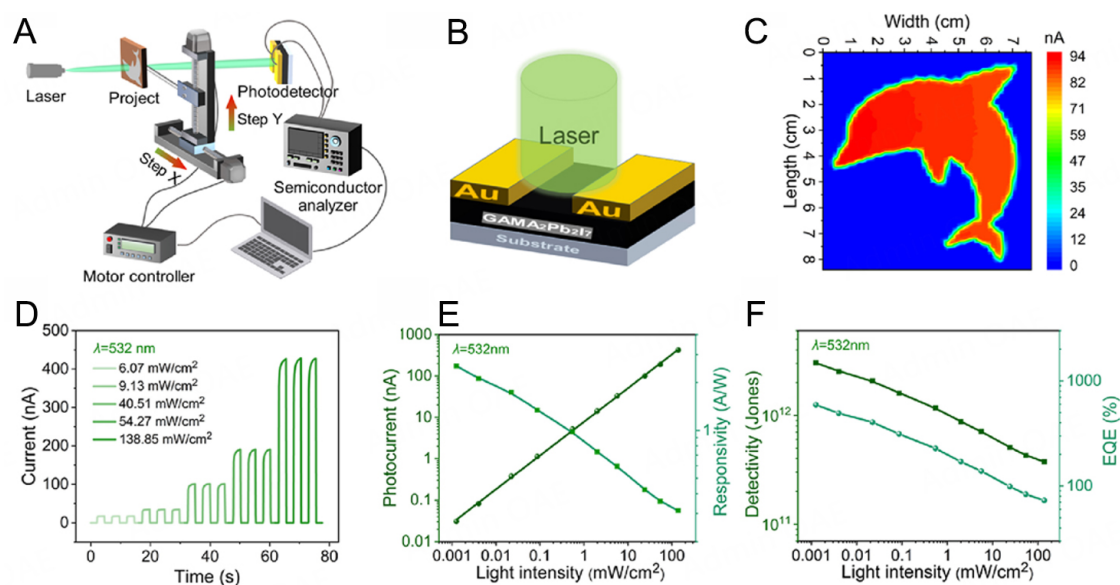
Figure 14. Schematic diagrams of (A) the imaging system and (B) (GA)(MA)$_2$Pb$_2$I$_7$ photodetector, (C) Imaging results of the (GA)(MA)$_2$Pb$_2$I$_7$ image sensor at 532 nm illumination. (D) The I-T curves, (E) Photocurrent and responsivity, and (F) Detectivity and EQE under 532 nm illumination. Reprinted with permission from ref.[27]: Copyright 2023, Elsevier.
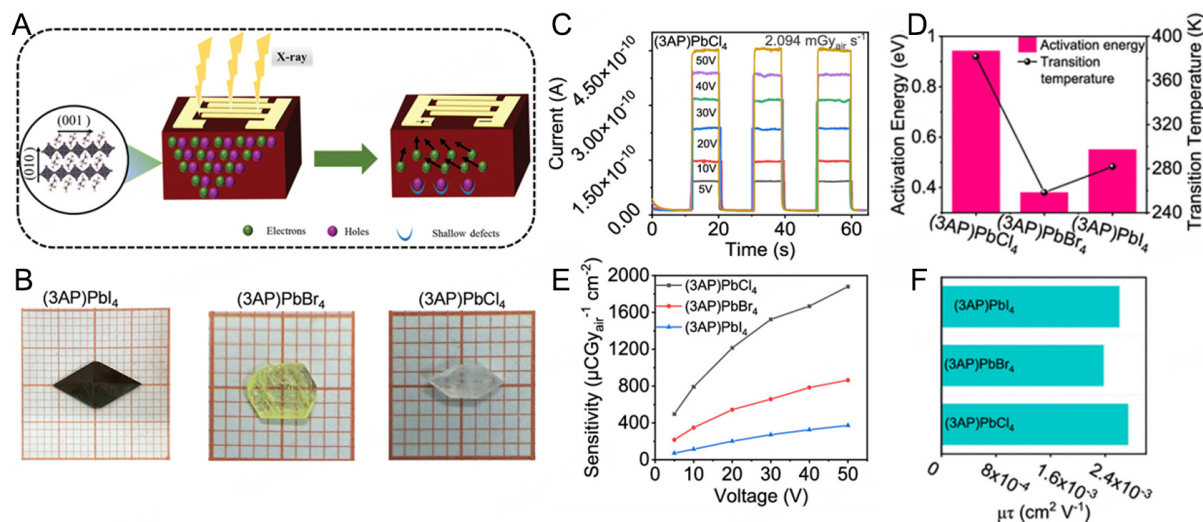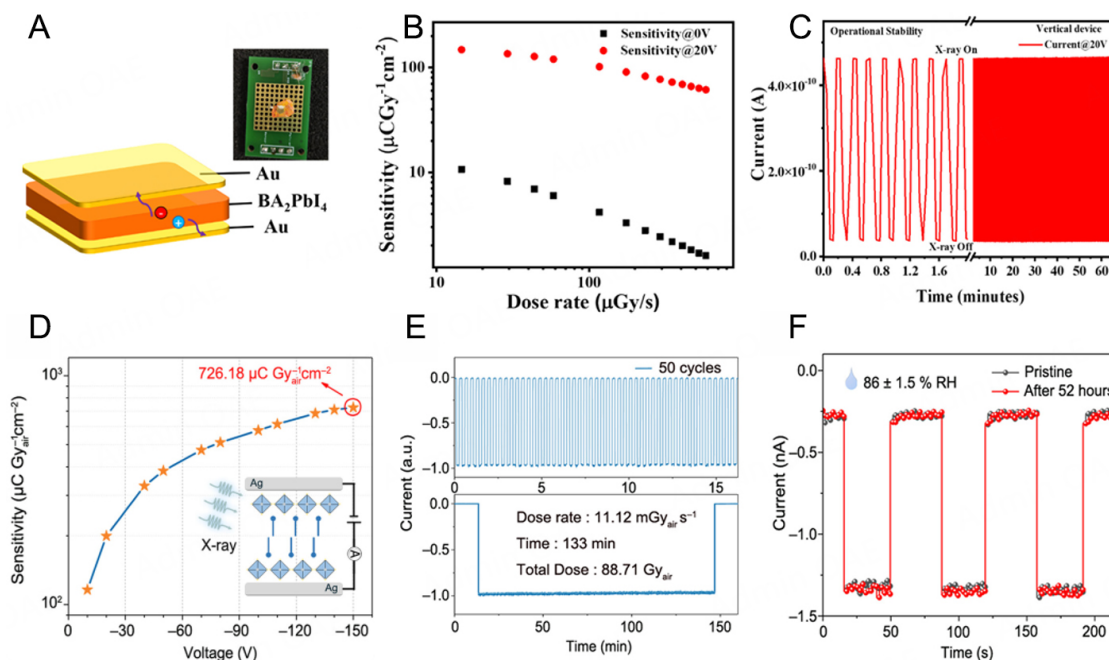
varying illumination levels, and (GA)(MA)$_2$Pb$_2$I$_7$ photodetectors at 532 nm incoming light with 9.82 nW could reach a high photoresponsivity of 2.54 A/W. In addition, the largest detectivity for the photodetectors is 3.04 × 10^{12} Jones and the corresponding external quantum efficiency (EQE) values are up to 592%. Aside from this, (GA)(MA)$_2$Pb$_2$I$_7$ single crystals show considerable operational and thermal stability which is beneficial to further practical applications. It has been reported that the (GA)(MA)$_2$Pb$_2$I$_7$ photodetector maintained 85.5% of its initial photocurrent after 1,000 s of operation at 532 nm illumination at ambient temperature and about 68% relative humidity, and also showed high thermal stability up to 260 °C[27]. These results showed the high-performance potential of 2D ACI phases for photodetection and imaging applications. The better crystal symmetry and addition of MA in the organic spacer layer result in a lower bandgap when compared to other phases with the same *n* value. The reduced dielectric confinement effect of these quantum-well structures in the ACI perovskites results in decreased exciton binding energy, which is advantageous in charge dynamics.

X-ray detectors

The 2D OIHP single crystals have great strengths in applications for X-ray detectors due to their exceptional defect tolerance, high averaged atomic number for X-ray absorption, restricted ion migration for stable current output, high resistivity for reduced noise, and excellent operational stability[25]. In the case of X-ray detectors, declining X-ray absorption with a sharp increase in the X-ray energy and potential damage from MeV radiation raises concerns for the stabilities and sensitivities of materials. The low X-ray absorptions in high-energy regions also cause the photocurrent drop, which is detrimental to the effective detection of MeV X-rays. Applying more bias can increase photocurrent, but the resulting increase in the dark current at high voltage is harmful to detecting performance. These undesirable events happen because of the polarization effect driven by ion migration, which commonly occurs in 3D perovskites[74,75]. Therefore, 2D perovskites with high ion migration diffusion barriers have a great deal of promise since they can be stable and sensitive for X-ray detection at high bias voltages[76].

In this prospect, RP phase $(BA)_2PbI_4$ single crystals have been demonstrated in X-ray detection applications, which are excellent candidates for X-ray detectors due to their low trap density, greater bulk resistivity, and increased carrier mobility and lifetime. Figure 15A and B shows the device illustration and sensitivity of a $(BA)_2PbI_4$ single crystal X-ray detector which is evaluated at 0 and 20 V mm^{-1}. With an irradiation dose of 14.6 μGy s^{-1}, the highest sensitivity was determined to be 148 μC Gy^{-1} cm^{-2} at 10 V mm^{-1} bias. Remarkably, it can work without any bias, exhibiting a sensitivity of 11 μC Gy^{-1} cm^{-2}. As shown in Figure 15C, $(BA)_2PbI_4$ X-ray detectors showed good operational stability with reproducibility of I-time curves before and after the stability test, which was measured at 10 V mm^{-1} electric field switched on/off repeatedly for approximately 1 h with 100 cycles. After a continuous pulsed X-ray exposure, $(BA)_2PbI_4$ X-ray detectors demonstrated remarkable stability with very little dark current drift at the off state[77]. $(BA)_2PbBr_4$ is also a typical 2D RP phase perovskite which is beneficial for maintaining structural stability and inhibiting dark current increase and drift at large applied biases due to less ion migration. Furthermore, $(BA)_2PbBr_4$ single crystal devices significantly minimize noise in the dark. As depicted in Figure 15D, sensitivity is evaluated at several biases, and at -150 V bias, a maximum measurement of 726.2 μC Gy$_{air}^{-1}$ cm^{-2} was detected. $(BA)_2PbBr_4$ devices demonstrated excellent low-energy X-ray detection performance and operational stability. Fifty cycles of repeated X-ray doses (50 keV, 564.7 μGy$_{air}$ s^{-1}) for stability test were performed on the $(BA)_2PbBr_4$ single crystal device at 0.061 V μm^{-1} in ambient conditions. This device was subjected to continuous X-ray radiation with 88.7 Gy$_{air}$ for 133 min, and no discernible degradation was seen [Figure 15E]. After 52 h of exposure at approximately 86% RH and a bias of -100 V without encapsulation, there is a small difference of 1.5% between the mean photocurrents before and after [Figure 15F]. $(BA)_2PbBr_4$ single crystal detectors can be suggested for radiation applications due to their broad detectable X-ray range and outstanding sensitivity in medium and high energy.

Recently, DJ perovskite single crystals have demonstrated better X-ray detector performance than RP counterparts[4,28]. From the study of DJ phase $(DGA)PbI_4$ single crystals, it is found that the smallest lattice distortion and increased hydrogen bonds in DJ perovskites strengthen lattice rigidity and diminish electron-phonon coupling to inhibit disordered scattering of carriers, leading to a significant improvement in carrier transport and stability[25]. The detecting mechanism of this device is depicted in Figure 16A. Significant electron-hole pairs are produced by the photoelectric effect when several photons enter the detector at once, and the electrodes (which are loaded with an electric field) gather these electron-hole pairs. Before recombination, the mobile majority carriers (electrons here) will continuously move between the electrodes due to the shallow defects that trap minority carriers (holes here). This leads to a high photoconductive gain. Ma *et al.* also reported DJ phase X-ray detectors with $(3AP)PbX_4$ (X = I, Br, and Cl), and Figure 16B shows photographs of these single crystals[4]. $(3AP)PbCl_4$ can respond to on-off X-ray radiation at a dosage of 2.094 mGy$_{air}$ s^{-1} with biases ranging from 5 to 50 V, as illustrated in Figure 16C. For $(3AP)PbX_4$ (X = Cl, Br, and I), the activation energy values were found to be 0.94, 0.38, and 0.55 eV, respectively. Notably, the activation energies of Cl-based crystals were high in the $(3AP)PbX_4$ series. Given that the Cl-based structures had better bonding than their Br- and I-based counterparts, including Pb-halogen bonding and hydrogen bonding, this suggests a comparatively reduced ion migration in the Cl-based crystals. In addition, the greatest transition temperature of 382 K was found in $(3AP)PbCl_4$ among all of the series [Figure 16D]. This suggests that $(3AP)PbCl_4$ will likely exhibit greater operational stability and be more resistant to ionic migration. For $(3AP)PbX_4$ (X = Cl, Br, and I), sensitivity was found to be 792, 349, and 115 μC Gy$_{air}^{-1}$ cm^{-2} at 10 V bias, and μτ values for holes were found to be 2.7×10^{-3}, 2.4×10^{-3}, and 2.6×10^{-3} cm^2 V^{-1}, respectively [Figure 16E and F][4]. These values are comparable to the value of 5.3×10^{-3} cm^2 V^{-1} for MAPbI$_3$[78], and a high μτ value suggests that the chemical has a great ability to extract charges when used for X-ray detectors. These advantages of 2D perovskite single crystals, such as a high mobility-lifetime product (μτ) and low trap density, have drawn attention in X-ray detection applications.

Figure 15. (A) Schematic diagram and fabricated device of the $(BA)_2PbI_4$ single crystal for X-ray detector. (B) X-ray dose rate and sensitivity at 0 and 20 V and (C) Operational stability under continuous X-ray exposure of vertical $(BA)_2PbI_4$ X-ray detectors. Reprinted with permission from ref.[77]: Copyright 2022, American Chemical Society. (D) Sensitivity under various biases, (E) operational stability over 50 repeated cycles of X-ray irradiation with 20 s time intervals and continuous irradiation at -10 V bias, and (F) Humidity stability at 86% ± 1.5% relative humidity (RH) of the $(BA)_2PbBr_4$ single crystal detector. Reprinted with permission from ref.[76]: Copyright 2023, Wiley-VCH GmbH.

Figure 16. (A) Schematic illustrations of the photoelectric process in the present $Au/(DGA)PbI_4/Au$ device under X-ray radiation. Reprinted with permission from ref.[25]: Copyright 2022, Wiley-VCH GmbH. (B) Photographs of DJ perovskite single crystals of $(3AP)PbX_4$ (X = I, Br, and Cl). (C) Current response of $(3AP)PbCl_4$ single-crystal X-ray detector under various voltages with 2.094 mGy_{air} s^{-1}. (D) Ion activation energy and transition temperature of $(3AP)PbX_4$ single crystals. (E) Sensitivity under various voltages (5-50 V). (F) Mobility-lifetime product ($\mu\tau$) for $(3AP)PbX_4$ single crystals. Reprinted with permission from ref.[4]: Copyright 2022, American Chemical Society.

In this section on optoelectronic applications of 2D single crystals, RP phase thin layers exhibit high narrowband excitonic light absorption, making them promising candidates for filterless narrowband

photodetectors. However, in RP phases, van der Waals forces allow two large spacer cations to interact with each other, along with hydrogen bonding occurring between the organic cation layers and the inorganic layers. As a result, despite RP perovskites demonstrating superior stability across various conditions, charge transport through the organic interlayers is hindered by the van der Waals gap between the layers. On the other hand, DJ perovskites, which incorporate diammonium cations, can reduce interlayer spacing, eliminate the van der Waals gap, and enhance structural stability, leading to benefits such as decreased ion migration and minimized quantum confinement effects. Notably, the improved lattice durability and shorter interlayer spacing of DJ perovskites facilitate more effective charge carrier transport. In contrast, while research on the application of ACI single crystals is limited, ACI single crystals exhibit significant potential for photodetection and imaging applications. The improved crystal symmetry and the inclusion of MA in the organic spacer layer contribute to a lower bandgap when compared to other phases with the same *n* value. The reduced dielectric confinement effect in these quantum-well structures within the ACI phase leads to decreased exciton binding energy, which is beneficial for charge dynamics.

CONCLUSIONS

The 2D OIHP single crystals have great potential owing to their enhanced stability, less ion migration, tuneable band structures, and flexible composition engineering. Furthermore, 2D OIHPs have strong anisotropic properties induced by unique quantum-well structures with controlled phase formation. In this review, phase-dependent materials design strategies are suggested with the selection of organic spacer cations and the tuning of inorganic layer thickness (*n*) within phases. These modifications in 2D OIHP crystal structures can significantly influence dielectric property, exciton binding energy, charge carrier behaviors, and bandgap energy compared with 3D perovskites. In addition, it is shown that 2D OIHP single crystals with different phases can play essential roles in developing high performance and stability-improved optoelectronic applications such as photodetectors and X-ray detectors with the possibility of their low dark current, high sensitivity, fewer grain boundaries, and low trap density. Each phase of 2D perovskites has distinct strengths in various applications, while it is still required to perform the phase-dependent stability investigation on 2D OIHP single crystals. Specifically, DJ phases have less distorted and more stable structures than the RP phase, and ACI phases have more 3D-like structures which can result in lower bandgap than other 2D phases with enhanced stability such as other 2D phases. Despite these reasons, it is not enough to clarify the comparison of stability and degradation mechanisms between phases, because of the few reports and challenges with the synthesis of phase-pure single crystals in DJ and ACI phases. In general, DJ or ACI phases are expected to have enhanced stability owing to the stronger bonding strength. However, there are conflicting arguments regarding the stability comparison between RP and DJ phases, especially concerning which phase exhibits better humidity and temperature stability. One report claims that RP has better ambient and thermal stability, with comparable photostability with DJ[55]. In contrast, another study indicates that DJ exhibits enhanced stability of humidity, heat and illumination[79]. Moreover, experiment studies on ACI phases are quite limited. Further comparative investigations should be performed, particularly under the same standard conditions. In the meantime, despite the potential of ACI phases that can control relatively lower bandgap energy, such as 1.5 eV below, suitable for high-performance optoelectronic device applications, its experimental approach to demonstrate the ACI device application has been less reported. Thus, further studies of 2D OIHP single crystals with diverse phase control are still required to exhibit excellent stability and performance, unlocking their potential for a wide range of applications.

DECLARATIONS

Original draft preparation, reviewing, and editing: Lee, S. M.
Reviewing and editing: Lian, M. M.; Ahn, S.H.; Yeon, D.J.; Zhang, Y.; Han, E.; Jang, Y.; Sul, J. H.

Availability of data and materials
Not applicable.

Conflicts of interest
Zhang, Y. is affiliated with Zhejiang Baima Lake Laboratory Co., Ltd, while the other authors have declared that they have no conflicts of interest.

Ethical approval and consent to participate
Not applicable.

Consent for publication
Not applicable.

REFERENCES

1. National Renewable Energy Laboratory. Best research-cell efficiency chart. Available from: https://www.nrel.gov/pv/cell-efficiency.html [Last accessed on 23 Dec 2024].
2. Chen, P.; Bai, Y.; Wang, S.; Lyu, M.; Yun, J. H.; Wang, L. In situ growth of 2D perovskite capping layer for stable and efficient perovskite solar cells. *Adv. Funct. Mater.* **2018**, *28*, 1706923. DOI
3. Choi, E.; Zhang, Y.; Soufiani, A. M.; et al. Exploration of sub-bandgap states in 2D halide perovskite single-crystal photodetector. *NPJ. 2D. Mater. Appl.* **2022**, *6*, 317. DOI
4. Ma, C.; Gao, L.; Xu, Z.; et al. Centimeter-sized 2D perovskitoid single crystals for efficient X-ray photoresponsivity. *Chem. Mater.* **2022**, *34*, 1699-709. DOI
5. Zhang, L.; Sun, C.; He, T.; et al. High-performance quasi-2D perovskite light-emitting diodes: from materials to devices. *Light. Sci. Appl.* **2021**, *10*, 61. DOI PubMed PMC
6. Hailegnaw, B.; Demchyshyn, S.; Putz, C.; et al. Flexible quasi-2D perovskite solar cells with high specific power and improved stability for energy-autonomous drones. *Nat. Energy.* **2024**, *9*, 677-90. DOI
7. Wu, G.; Liang, R.; Ge, M.; Sun, G.; Zhang, Y.; Xing, G. Surface passivation using 2D perovskites toward efficient and stable perovskite solar cells. *Adv. Mater.* **2022**, *34*, e2105635. DOI
8. Leung, T. L.; Ahmad, I.; Syed, A. A.; Ng, A. M. C.; Popović, J.; Djurišić, A. B. Stability of 2D and quasi-2D perovskite materials and devices. *Commun. Mater.* **2022**, *3*, 285. DOI
9. Zheng, H.; Liu, G.; Zhu, L.; et al. The effect of hydrophobicity of ammonium salts on stability of quasi-2D perovskite materials in moist condition. *Adv. Energy. Mater.* **2018**, *8*, 1800051. DOI
10. Sheng, X.; Li, Y.; Xia, M.; Shi, E. Quasi-2D halide perovskite crystals and their optoelectronic applications. *J. Mater. Chem. A.* **2022**, *10*, 19169-83. DOI
11. Sun, S.; Lu, M.; Gao, X.; et al. 0D perovskites: unique properties, synthesis, and their applications. *Adv. Sci.* **2021**, *8*, e2102689. DOI PubMed PMC
12. Lin, H.; Zhou, C.; Tian, Y.; Siegrist, T.; Ma, B. Low-dimensional organometal halide perovskites. *ACS. Energy. Lett.* **2018**, *3*, 54-62. DOI
13. Kieslich, G.; Sun, S.; Cheetham, A. K. Solid-state principles applied to organic-inorganic perovskites: new tricks for an old dog. *Chem. Sci.* **2014**, *5*, 4712-5. DOI

14. Travis, W.; Glover, E. N. K.; Bronstein, H.; Scanlon, D. O.; Palgrave, R. G. On the application of the tolerance factor to inorganic and hybrid halide perovskites: a revised system. *Chem. Sci.* **2016**, *7*, 4548-56. DOI PubMed PMC

15. Mao, L.; Stoumpos, C. C.; Kanatzidis, M. G. Two-dimensional hybrid halide perovskites: principles and promises. *J. Am. Chem. Soc.* **2019**, *141*, 1171-90. DOI PubMed

16. Keldysh, L. Excitons in semiconductor-dielectric nanostructures. *Phys. Status. Solidi. A.* **1997**, *1*, 3-12. DOI

17. Keldysh, L. V. Coulomb interaction in thin semiconductor and semimetal films; 2023. pp. 155-8. DOI

18. Rytova, N. S. Screened potential of a point charge in a thin film. Moscow University Physics Bulletin; 1967. DOI

19. Chakraborty, R.; Nag, A. Dielectric confinement for designing compositions and optoelectronic properties of 2D layered hybrid perovskites. *Phys. Chem. Chem. Phys.* **2021**, *23*, 82-93. DOI PubMed

20. Pedesseau, L.; Sapori, D.; Traore, B.; et al. Advances and promises of layered halide hybrid perovskite semiconductors. *ACS. Nano.* **2016**, *10*, 9776-86. DOI

21. Qian, J.; Xu, B.; Tian, W. A comprehensive theoretical study of halide perovskites ABX3. *Org. Electron.* **2016**, *37*, 61-73. DOI

22. Wu, G.; Liang, R.; Zhang, Z.; Ge, M.; Xing, G.; Sun, G. 2D hybrid halide perovskites: structure, properties, and applications in solar cells. *Small* **2021**, *17*, e2103514. DOI

23. Soe, C. M. M.; Stoumpos, C. C.; Kepenekian, M.; et al. New type of 2D perovskites with alternating cations in the interlayer space, $(C(NH_2)_3)(CH_3NH_3)nPb_nI_{3n+1}$: structure, properties, and photovoltaic performance. *J. Am. Chem. Soc.* **2017**, *139*, 16297-309. DOI

24. Shen, Y.; Liu, Y.; Ye, H.; et al. Centimeter-sized single crystal of two-dimensional halide perovskites incorporating straight-chain symmetric diammonium ion for X-Ray detection. *Angew. Chem. Int. Ed.* **2020**, *59*, 14896-902. DOI

25. Zhang, B.; Zheng, T.; You, J.; et al. Electron-phonon coupling suppression by enhanced lattice rigidity in 2D perovskite single crystals for high-performance X-Ray detection. *Adv. Mater.* **2023**, *35*, e2208875. DOI

26. Fu, D.; Hou, Z.; He, Y.; et al. Formamidinium perovskitizers and aromatic spacers synergistically building bilayer Dion-Jacobson perovskite photoelectric bulk crystals. *ACS. Appl. Mater. Interfaces.* **2022**, *14*, 11690-8. DOI

27. Li, Y.; Lai, Z.; Meng, Y.; et al. High-performance photodetectors based on two-dimensional perovskite crystals with alternating interlayer cations. *J. Materiomics.* **2023**, *9*, 817-23. DOI

28. Mao, L.; Ke, W.; Pedesseau, L.; et al. Hybrid Dion-Jacobson 2D lead iodide perovskites. *J. Am. Chem. Soc.* **2018**, *140*, 3775-83. DOI

29. Peng, W.; Yin, J.; Ho, K. T.; et al. Ultralow Self-doping in two-dimensional hybrid perovskite single crystals. *Nano. Lett.* **2017**, *17*, 4759-67. DOI

30. Qian, C. X.; Wang, M. Z.; Lu, S. S.; Feng, H. J. Fabrication of 2D perovskite $(PMA)_2PbI_4$ crystal and Cu ion implantation improved X-ray detector. *Appl. Phys. Lett.* **2022**, *120*, 011901. DOI

31. Wang, H.; Wang, Q.; Ning, M.; et al. Synthesis of centimeter-size two-dimensional hybrid perovskite single crystals with tunable, pure, and stable luminescence. *RSC. Adv.* **2023**, *13*, 22886-94. DOI PubMed PMC

32. He, X.; Wang, Y.; Li, K.; et al. Oriented growth of ultrathin single crystals of 2D Ruddlesden-Popper hybrid lead iodide perovskites for high-performance photodetectors. *ACS. Appl. Mater. Interfaces.* **2019**, *11*, 15905-12. DOI

33. Lédée, F.; Trippé-Allard, G.; Diab, H.; et al. Fast growth of monocrystalline thin films of 2D layered hybrid perovskite. *CrystEngComm* **2017**, *19*, 2598-602. DOI

34. Yan, W.; Duan, B.; Song, Y.; et al. Self-absorption and investigation of excited carrier dynamics in two-dimensional perovskite scintillator. *Appl. Phys. Lett.* **2024**, *124*, 053101. DOI

35. Tian, H.; Zhao, L.; Wang, X.; et al. Extremely low operating current resistive memory based on exfoliated 2D perovskite single crystals for neuromorphic computing. *ACS. Nano.* **2017**, *11*, 12247-56. DOI

36. Zhang, D.; Wei, X.; Wang, F.; Tang, H.; Deng, W.; Liu, J. Biphasic interfacial swimming top-down growth of Ruddlesden-Popper halide perovskite single-crystal sheets with few defects. *Adv. Opt. Mater.* **2024**, *12*, 2400617. DOI

37. Xiao, X.; Dai, J.; Fang, Y.; et al. Suppressed ion migration along the in-plane direction in layered perovskites. *ACS. Energy. Lett.* **2018**, *3*, 684-8. DOI

38. Dong, K.; Yang, X.; Yao, F.; et al. Spacer conformation induced multiple hydrogen bonds in 2D perovskite toward highly efficient optoelectronic devices. *Adv. Mater.* **2024**, *36*, e2313889. DOI

39. Hong, E.; Li, Z.; Yan, T.; Fang, X. Surface-tension-dominant crystallization of 2D perovskite single crystals for vertically oriented hetero-/homo-structure photodetectors. *Nano. Lett.* **2022**, *22*, 8662-9. DOI

40. Cinquino, M.; Fieramosca, A.; Mastria, R.; et al. Managing growth and dimensionality of quasi 2D perovskite single-crystalline flakes for tunable excitons orientation. *Adv. Mater.* **2021**, *33*, e2102326. DOI PubMed PMC

41. Stoumpos, C. C.; Cao, D. H.; Clark, D. J.; et al. Ruddlesden-Popper hybrid lead iodide perovskite 2D homologous semiconductors. *Chem. Mater.* **2016**, *28*, 2852-67. DOI

42. Cinquino, M.; Polimeno, L.; Lerario, G.; et al. One-step synthesis at room temperature of low dimensional perovskite single crystals with high optical quality. *J. Lumin.* **2020**, *221*, 117079. DOI

43. Paritmongkol, W.; Dahod, N. S.; Stollmann, A.; et al. Synthetic variation and structural trends in layered two-dimensional alkylammonium lead halide perovskites. *Chem. Mater.* **2019**, *31*, 5592-607. DOI

44. Soe, C. M. M.; Nagabhushana, G. P.; Shivaramaiah, R.; et al. Structural and thermodynamic limits of layer thickness in 2D halide perovskites. *Proc. Natl. Acad. Sci. USA.* **2019**, *116*, 58-66. DOI PubMed PMC

45. Raghavan, C. M.; Chen, T. P.; Li, S. S.; et al. Low-threshold lasing from 2D homologous organic-inorganic hybrid Ruddlesden-Popper perovskite single crystals. *Nano. Lett.* **2018**, *18*, 3221-8. DOI

46.   Fateev, S. A.; Petrov, A. A.; Ordinartsev, A. A.; Grishko, A. Y.; Goodilin, E. A.; Tarasov, A. B. Universal strategy of 3D and 2D hybrid perovskites single crystal growth via in situ solvent conversion. *Chem. Mater.* **2020**, *32*, 9805-12. DOI

47.   Liu, Y.; Ye, H.; Zhang, Y.; et al. Surface-Tension-controlled crystallization for high-quality 2D perovskite single crystals for ultrahigh photodetection. *Matter* **2019**, *1*, 465-80. DOI

48.   Rahil, M.; Ansari, R. M.; Prakash, C.; Islam, S. S.; Dixit, A.; Ahmad, S. Ruddlesden-Popper 2D perovskites of type $(C_6H_9C_2H_4NH_3)_2(CH_3NH_3)_{n-1}Pb_nI_{3n+1}$ (n = 1-4) for optoelectronic applications. *Sci. Rep.* **2022**, *12*, 2176. DOI PubMed PMC

49.   Gao, L.; Li, X.; Traoré, B.; et al. m-Phenylenediammonium as a new spacer for Dion-Jacobson two-dimensional perovskites. *J. Am. Chem. Soc.* **2021**, *143*, 12063-73. DOI

50.   Zheng, Y.; Niu, T.; Qiu, J.; et al. Oriented and uniform distribution of Dion-Jacobson phase perovskites controlled by quantum well barrier thickness. *Solar. RRL.* **2019**, *3*, 1900090. DOI

51.   Blancon, J. C.; Tsai, H.; Nie, W.; et al. Extremely efficient internal exciton dissociation through edge states in layered 2D perovskites. *Science* **2017**, *355*, 1288-92. DOI

52.   Gan, L.; Li, J.; Fang, Z.; He, H.; Ye, Z. Effects of organic cation length on exciton recombination in two-dimensional layered lead iodide hybrid perovskite crystals. *J. Phys. Chem. Lett.* **2017**, *8*, 5177-83. DOI

53.   Huang, P.; Kazim, S.; Wang, M.; Ahmad, S. Toward phase stability: Dion-Jacobson layered perovskite for solar cells. *ACS. Energy. Lett.* **2019**, *4*, 2960-74. DOI

54.   Ghosh, D.; Acharya, D.; Pedesseau, L.; et al. Charge carrier dynamics in two-dimensional hybrid perovskites: Dion-Jacobson *vs.* Ruddlesden-Popper phases. *J. Mater. Chem. A* **2020**, *8*, 22009-22. DOI

55.   Vasileiadou, E. S.; Wang, B.; Spanopoulos, I.; Hadar, I.; Navrotsky, A.; Kanatzidis, M. G. Insight on the stability of thick layers in 2D Ruddlesden-Popper and Dion-Jacobson lead iodide perovskites. *J. Am. Chem. Soc.* **2021**, *143*, 2523-36. DOI PubMed

56.   Li, W.; Feng, X.; Guo, K.; et al. Prominent free charges tunneling through organic interlayer of 2D perovskites. *Adv. Mater.* **2023**, *35*, e2211808. DOI

57.   Traore, B.; Pedesseau, L.; Assam, L.; et al. Composite nature of layered hybrid perovskites: assessment on quantum and dielectric confinements and band alignment. *ACS. Nano.* **2018**, *12*, 3321-32. DOI

58.   Kepenekian, M.; Traore, B.; Blancon, J. C.; et al. Concept of lattice mismatch and emergence of surface states in two-dimensional hybrid perovskite quantum wells. *Nano. Lett.* **2018**, *18*, 5603-9. DOI

59.   Li, F.; Zhang, J.; Jo, S.; et al. Vertical orientated Dion-Jacobson Quasi-2D perovskite film with improved photovoltaic performance and stability. *Small. Methods.* **2020**, *4*, 1900831. DOI

60.   Ghosh, S.; Pradhan, B.; Zhang, Y.; et al. Investigation of many-body exciton recombination and optical anisotropy in two-dimensional perovskites having different layers with alternating cations in the interlayer space. *J. Phys. Chem. C* **2021**, *125*, 7799-807. DOI

61.   Li, P.; Liang, C.; Liu, X. L.; et al. Low-dimensional perovskites with diammonium and monoammonium alternant cations for high-performance photovoltaics. *Adv. Mater.* **2019**, *31*, e1901966. DOI

62.   Stoumpos, C. C.; Mao, L.; Malliakas, C. D.; Kanatzidis, M. G. Structure-band gap relationships in hexagonal polytypes and low-dimensional structures of hybrid tin iodide perovskites. *Inorg. Chem.* **2017**, *56*, 56-73. DOI PubMed

63.   Gao, L.; Luo, X.; Sun, J. L.; Li, Q.; Yan, Q. Room-temperature solvent evaporation induced crystallization: a general strategy for growth of halide perovskite single crystals by applying the Le Chatelier's Principle. *Small* **2023**, *19*, e2303687. DOI

64.   Shi, D.; Adinolfi, V.; Comin, R.; et al. Low trap-state density and long carrier diffusion in organolead trihalide perovskite single crystals. *Science* **2015**, *347*, 519-22. DOI

65.   Cheng, Z.; Liu, K.; Yang, J.; et al. High-performance planar-type ultraviolet photodetector based on high-quality $CH_3NH_3PbCl_3$ perovskite single crystals. *ACS. Appl. Mater. Interfaces.* **2019**, *11*, 34144-50. DOI

66.   Liu, Y.; Zhang, Y.; Yang, Z.; et al. Low-temperature-gradient crystallization for multi-inch high-quality perovskite single crystals for record performance photodetectors. *Mater. Today.* **2019**, *22*, 67-75. DOI

67.   Zhang, Y.; Liu, Y.; Yang, Z.; Liu, S. F. High-quality perovskite $MAPbI_3$ single crystals for broad-spectrum and rapid response integrate photodetector. *J. Energy. Chem.* **2018**, *27*, 722-7. DOI

68.   Muljarov, E. A.; Tikhodeev, S. G.; Gippius, N. A.; Ishihara, T. Excitons in self-organized semiconductor/insulator superlattices: PbI-based perovskite compounds. *Phys. Rev. B. Condens. Matter.* **1995**, *51*, 14370-8. DOI PubMed

69.   Tu, Y.; Xu, Y.; Li, J.; et al. Ultrathin single-crystalline 2D perovskite photoconductor for high-performance narrowband and wide linear dynamic range photodetection. *Small* **2020**, *16*, e2005626. DOI

70.   Liu, Y.; Zhang, Y.; Yang, Z.; et al. Multi-inch single-crystalline perovskite membrane for high-detectivity flexible photosensors. *Nat. Commun.* **2018**, *9*, 5302. DOI PubMed PMC

71.   Li, J.; Wang, J.; Ma, J.; et al. Self-trapped state enabled filterless narrowband photodetections in 2D layered perovskite single crystals. *Nat. Commun.* **2019**, *10*, 806. DOI PubMed PMC

72.   Xiang, M.; Dai, S.; Li, S.; et al. Comparative analysis of different ammonium-based cations in 2D DJ-type perovskite single crystals for high-performance planar photodetectors. *J. Phys. Chem. C* **2024**, *128*, 2928-36. DOI

73.   Zhang, Y.; Liu, Y.; Xu, Z.; Yang, Z.; Liu, S. F. 2D perovskite single crystals with suppressed ion migration for high-performance planar-type photodetectors. *Small* **2020**, *16*, e2003145. DOI

74.   Meloni, S.; Moehl, T.; Tress, W.; et al. Ionic polarization-induced current-voltage hysteresis in $CH_3NH_3PbX_3$ perovskite solar cells. *Nat. Commun.* **2016**, *7*, 10334. DOI PubMed PMC

75.   Lin, Y.; Bai, Y.; Fang, Y.; Wang, Q.; Deng, Y.; Huang, J. Suppressed ion migration in low-dimensional perovskites. *ACS. Energy.*

Lett. **2017**, *2*, 1571-2. DOI

76. Xu, X.; Wu, Y.; Zhang, Y.; et al. Two-dimensional perovskite single crystals for high-performance X-ray imaging and exploring MeV X-ray detection. *Energy. Environ. Mater.* **2024**, *7*, e12487. DOI

77. Ghosh J, Afroz MA, Alghamdi S, Sellin PJ, Satapathi S. Efficient and highly stable X-ray detection and imaging using 2D $(BA)_2PbI_4$ perovskite single crystals. *ACS. Photonics.* **2022**, *9*, 3529-39. DOI

78. Huang, Y.; Qiao, L.; Jiang, Y.; et al. A-site cation engineering for highly efficient $MAPbI_3$ single-crystal X-ray detector. *Angew. Chem. Int. Ed.* **2019**, *58*, 17834-42. DOI

79. Gangadharan D, Ma D. Searching for stability at lower dimensions: current trends and future prospects of layered perovskite solar cells. *Energy. Environ. Sci.* **2019**, *12*, 2860-89. DOI